U–Pb Zircon Geochronology and Geochemistry of Some Plutonic Rocks from the Afif Terrane of Saudi Arabia, Arabian Shield: Implications for Crustal Evolution

Hesham M. Harbi

Abstract

The study areas (Bulghah and Hamimuah) are located in the Afif terrane between the Halaban–Zarghat fault zone and Ar Rika fault zone. They consist of many gabbroic to granitic I-type intrusions emplaced into Neoproterozoic volcanosedimentary rocks and are intruded by Neoproterozoic A-type granites. The studied plutonic rocks are I-type magmatic rocks, calk-alkaline, metaluminous to slightly peraluminous (A/CNK > 1.2), formed in a volcanic arc setting. On a primitive mantle-normalized spider diagrams, almost all rocks show a significant Nb–Ta–Ti depletions relative to K and La, which is typical of magmatism from a subduction zone tectonic setting. Geochemical features of the mafic intrusion (gabbro and diorite) are comparable to those of the arc-metavolcanic calc-alkaline rocks of the Arabian Shield, which were produced by partial melting of plagioclase- or spinel-peridotite in the upper most mantle <80 km deep in an intra-oceanic island arc. This suggests that the mafic intrusive rocks of Bulghah and Humaymah represent the plutonic equivalents of the Arabian Shield arc metavolcanic calc-alkaline rocks. The compositional variations from granodiorite to monzogranite of Bulghah and Humaymah suggest various degree of fractional crystallization of feldspar, biotite and amphibole. Y/Nb with Th/Nb, Th/Ta and Ce/Pb relationships indicate that the granodiorite and monzogranite were generated by a mafic parental magma contaminated with crustal materials, and controlled by fractional crystallization. Zircon U–Pb dating indicates that the mafic intrusive rocks from Bulghah and Humaymah, Saudi Arabia were formed at ∼670 Ma, whereas the granitoid I-type intrusions were formed between 661 ± 5 and 643 ± 4 Ma, confirming the importance of the 640–700 Ma crust forming event in Saudi Arabia.

6.1 Introduction

The Arabian Shield (AS, Fig. 6.1) consists of Neoproterozoic juvenile tectonostratigraphic island-arc terranes formed by subduction within and around the Mozambique Ocean between 850 and 550 Ma in the framework of the Gondwana supercontinent assembly (Stern 1994; Nehlig et al. 2002; Stern and Johnson 2010). These terranes are joined by ophiolite-decorated sutures (Stoeser and Camp 1985; Johnson and Woldehaimanot 2003). The AS is divided into at least five tectonostratigraphic terranes (Fig. 6.1; Stoeser and Camp 1985): Midyan, Hijaz, Asir, Ar Ryan and Afif with some workers (e.g., Johnson and Woldehaimanot 2003) discussed the possibility of three more terranes (Jiddah, Ad Dawadimi and Khida). All terranes (except Khida; Stacey and Agar 1985; Stoeser and Frost 2006) are regarded as Neoproterozoic oceanic arcs, including fore-arc and/or backarc crust and ophiolites (Dilek and Ahmed 2003; Stoeser and Frost 2006).

The evolution of the AS terranes records three main tectonic stages of intra-oceanic subduction (850–700 Ma), collision and terrain amalgamation (700–635 Ma), and tectonic escape, strike-slip faulting and extension (635–550 Ma) of the newly formed continental crust (Genna et al. 2002; Johnson and Woldehaimanot 2003; Be'eri-Shlevin et al. 2009; Eyal et al. 2010; Stern and Johnson 2010; Johnson et al. 2011). The volcanic arc crust range in composition from tholeiitic, through calc-alkaline to late high-K suites (Robool et al. 1983). Syn-to Post-collisional

H. M. Harbi (✉)
Department of Mineral Resources and Rocks, Faculty of Earth Sciences, King Abdulaziz University, P.O. Box 80206 Jeddah, 21589, Saudi Arabia
e-mail: harbihesham@hotmail.com
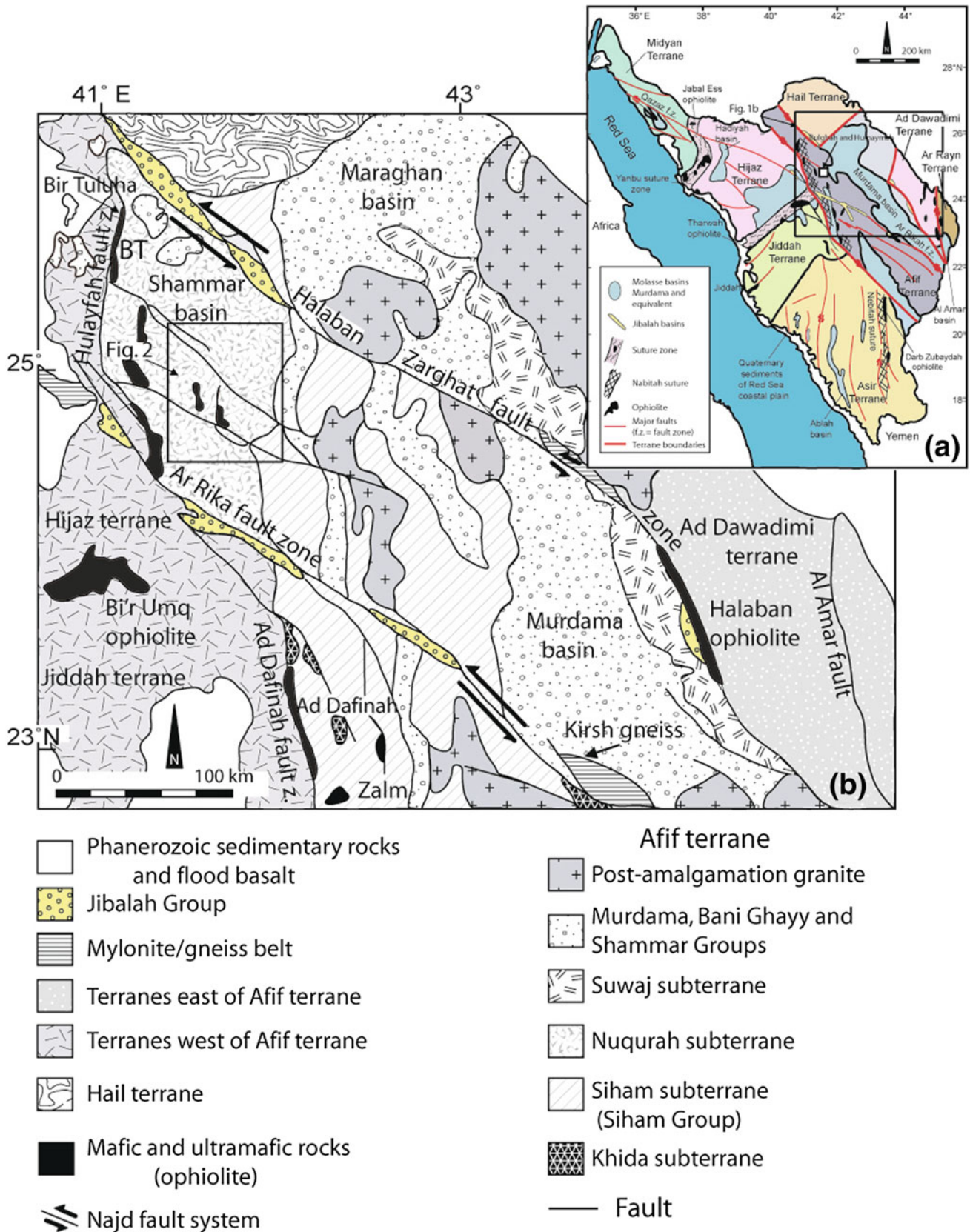
Fig. 6.1 **a** General geologic map of the Arabian Shield showing major tectonostratigraphic terranes, ophiolite belts, sutures, fault zones and post-accretionary basins in the Arabian Shield of western Saudi Arabia (modified after Nehlig et al. 2002; Johnson and Woldenhaimanot 2003; Stern and Johnson 2010). Numbers are locations of the I-type intrusive rocks represented in geochemical Figures as follows: (1) Bulghah and Humaymah, (2) Sukhaybarat, (3) Jabal Ghadarah, and (4) Makkah Suite. **b** Geological sketch map of the Afif Terrane and adjacent parts of the Arabian Shield showing location of the study area (modified after Johnson and Kattan 1999)

calc-alkaline to alkaline I-type granites intruded by Post-collisional K-rich alkaline to peralkaline A-type granites (e.g., Ali et al. 2009, 2012; Be'eri-Shlevin et al. 2009; Eyal et al. 2010; Moreno et al. 2014; Moghazi et al. 2012).

I-type granitoids (Cryogenian and Early Ediacaran) are major components of the ANS (Moussa et al. 2008; Johnson et al. 2011). Geochemical studies reveal that they are metaluminous to slightly peraluminous, calc-alkaline, subduction-related intrusives (Pearce et al. 1984; Maniar and Piccoli 1989; Jarrar et al. 2003; Moussa et al. 2008; Be'eri-Shlevin et al. 2009; Ali et al. 2015; Robinson et al. 2015), formed synchronously with the formation of large molasse basins (Genna et al. 2002; Johnson 1998; Nehlig et al. 2002; Stern and Johnson 2010). The orogenic phase was then followed by continued convergence and the development of regionally extensive strike-slip fault (escape tectonics) from 610 to 525 Ma (Greiling et al. 1994; Stern 1994; Genna et al. 2002; Johnson et al. 2011; Robinson et al. 2014).

Intrusion of post-collisional alkaline to peralkaline rocks (A-type granites) and development of extensive pull-apart basins during the final suturing of the Arabian-Nubian Shield and the formation of subsequent extensional basins (Greiling et al. 1994; Johnson 1998, 2003; Wilde and Youssef 2000; Nehlig et al. 2002; Johnson et al. 2011). The alkaline granites constitute about 2% of the Arabian–Nubian Shield and represent one of the largest fields of alkaline granites on Earth (Stoeser 1986; Liégeois and Stern 2010; Johnson et al. 2011). Petrogenetic models for the generation of A-type alkaline granites range from partial melting of the lower crust to extreme differentiation of mantle-derived tholeiitic or alkaline basaltic magma (Bonin and Giret 1990; Turner et al. 1992; Collins et al. 1992; Frost and Frost 1997; Patiño Douce 1997; Mushkin et al. 2003; Huang et al, 2011). Assimilation of older crustal material into mantle derived granitic magma is plausible model to account for the petrogenesis of such rocks (Eby 1990, 1992; Kemp et al. 2006; Zhang et al. 2012).

This paper will present results of U–Pb zircon geochronology and whole-rock geochemical data of some plutonic rocks from Bulghah and Humaymah areas (west of the Afif terrane) of Saudi Arabia. While gold is mined from Bulghah area since 2001, it is still under evaluation and development by Ma'aden Co. in the Humaymah area. In these areas, gold is spatially associated with some intrusive rocks intruding the layered volanosedimentary the Hulayfah/Siham and Murdamah group rocks. These intrusive rocks can be grouped into two groups; older mafic to intermediate gabbro-diorite and younger intermediate to felsic tonalite-granodiorite intrusive bodies. These data will be used to clarify the magma sources for these rocks, and to assess fractional crystallization as a possible petrogenetic mechanism for the formation of these rocks (Miller 1985; Secchi et al. 1991; Teixeira et al. 2012; Wang et al. 2014).

6.2 Geology Background and Petrography

The two selected areas (Bulghah and Humaymah) for the present study are located in the Afif terrane (Figs. 6.1 and 6.2). The Afif terrane is one of the largest terranes in the Arabian Shield. Much of the recent researches on the shield in the last 15 years, Johnson and Kattan (1999) addressed the composite nature of the Afif terrane in age and provenance, mainly based on detailed mapping, Pb-isotope systematics and U–Pb zircon geochronology (e.g., Stacey and Hedge 1984; Stacey and Agar 1985; Agar 1985, 1988; Agar et al. 1992). Based on these studies, the Afif terrane was divided into four possible subterranes including the Khida, Nuqrah, Siham, and Suwaj (Fig. 6.2). While the Khida subterrane represents remnants of the Archean to Paleoproterozoic continental rocks, the Nuqrah, Siham, and Suwaj subterranes and the post-amalgamation assemblages (Murdama and Bani Ghayy groups) represent the Neoproterozoic volcanic/magmatic arc-subterranes (Johnson and Kattan 1999). Agar et al. (1992) reported 1.7 Ga zircon ages for pre-Neoproterozoic sources in the Khida subterrane. The ophiolite assemblages (mafic/ultramafic rocks) represent the oldest Neoproterozoic rocks in the study areas. A plagiogranite dyke in serpentinized peridotites from a near vicinity to the study area in the Bir Tuluha ophiolite (Fig. 6.2) yielded U–Pb zircon ages from 843 to 821 Ma (Pallister et al. 1988). The mafic-ultramafic rocks are represented by gabbro, metabasalt, serpentinites, listvenites and amphibolites. The Siham group (Fig. 6.2) is unconformably overlain by the volcanosedimentary rocks of the Bani Ghayy group (Stacey and Agar 1985). The Siham group is metamorphosed to greenschist facies and composed mainly of volcanosedimentary assemblages. It is composed mainly of basaltic lava range from tholeiitic to calc-alkaline and has affinity with lavas in active continental margins (Agar 1986). The sedimentary rocks of Siham group are represented by lithic sandstone, shale and conglomerate. The age of the Siham group is constrained at $\sim 746 \pm 10$ Ma (Agar et al. 1992) from a granodiorite sample from Naim complex which intruded the Siham group. The Bani Ghayy group in the study area consists of unmetamorphosed sandstone, conglomerate, limestone, basalt and rhyolite. In the western part of the study area (Fig. 6.2), the Bani Ghayy and Murdama groups are separated by a thrust fault. Some workers considered the two groups to be equivalent because they are similar in age and lithology (Brown et al. 1989). The two groups suggested to be deposited during and soon after the Nabitah orogeny (680–640 Ma, Johnson et al. 2011). Stacey and Agar (1985) reported a U–Pb zircon age of 620 ± 5 Ma for a rhyolite sample from the Bani Ghayy group and a volcanic sample from Murdama group yielded a U–Pb zircon age of 625 ± 4 (Kusky and Matsah 2003)..
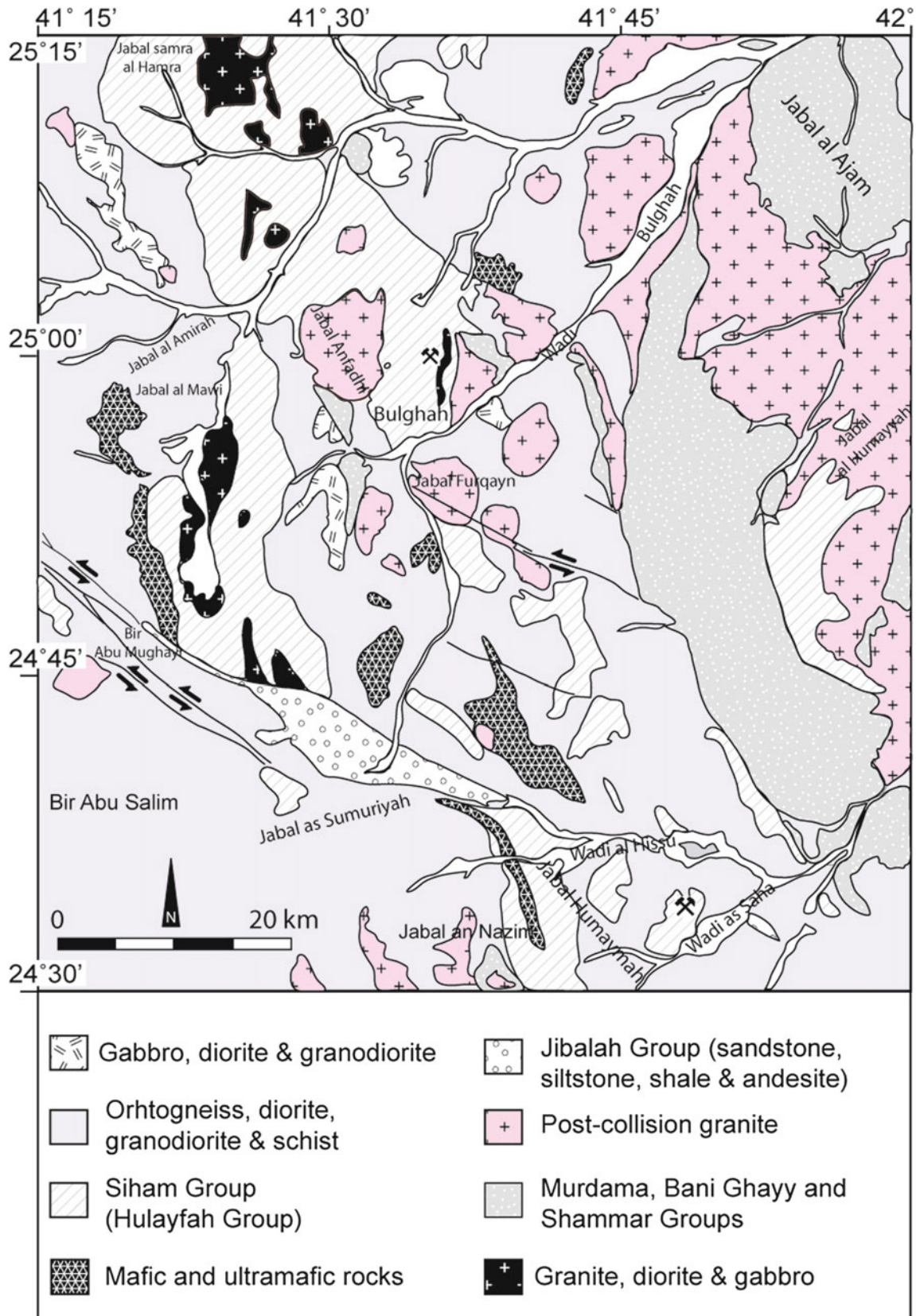
Fig. 6.2 Geological map showing the study areas (Bulghah and Humaymah) modified from the Geological maps 1:250000 of the Al Hissu quadrangle, sheet 24 E (Delfour 1981) and the Nuqrah quadrangle, sheet 25 E (Delfour 1977)

Table 6.1 SHRIMP Th-U-Pb zircon data for samples from Saudi Arabia

Spot No.	U ppm	Th ppm	Th/U	204Pb/206Pb	208Pb/232Th	% error	f206 %	207Pb*/206Pb*	% error	206Pb*/238U	% error	207Pb*/235U	% error	208Pb/232Th	% error	err corr	AGE 204 correction 208Pb/232Th	1σ error	207Pb*/206Pb*	1σ error	206Pb*/238U	1σ error
Sample B139 (Bulgah diorite)																						
B139.1	115	39	0.34	0.00019	0.0356	2.76	0.33	0.0597	0.001	0.113	0.002	0.930	0.028	0.033	3.71	0.57	663	25	591	53	691	11
B139.2	78	21	0.27	0.00021	0.0361	3.33	0.37	0.0592	0.001	0.111	0.002	0.910	0.027	0.033	3.85	0.56	655	25	575	53	681	10
B139.3**	102	51	0.50	0.00005	0.0359	2.48	0.08	0.0632	0.001	0.116	0.002	1.010	0.025	0.035	2.54	0.63	704	18	715	40	707	10
B139.4	69	24	0.35	0.00056	0.0355	3.32	0.99	0.0564	0.003	0.110	0.002	0.858	0.052	0.029	8.63	0.29	578	50	468	129	675	11
B139.5	114	31	0.27	0.00033	0.0371	2.85	0.58	0.0583	0.001	0.111	0.002	0.896	0.022	0.032	2.93	0.62	640	19	543	42	681	10
B139.6	138	38	0.28	0.00027	0.0378	2.79	0.47	0.0609	0.002	0.112	0.002	0.938	0.041	0.034	7.17	0.35	674	48	634	88	683	10
B139.7	133	41	0.30	0.00004	0.0348	2.82	0.07	0.0630	0.001	0.108	0.002	0.941	0.024	0.035	3.18	0.61	702	22	708	42	663	10
B139.8	95	30	0.31	0.00010	0.0343	3.27	0.17	0.0647	0.001	0.112	0.002	0.997	0.028	0.036	3.65	0.61	705	26	764	47	683	11
B139.9**	136	70	0.52	0.00001	0.0344	2.37	0.02	0.0658	0.001	0.111	0.002	1.003	0.022	0.035	2.34	0.67	686	16	800	35	676	10
B139.10	113	54	0.48	0.00032	0.0361	2.54	0.56	0.0591	0.003	0.113	0.002	0.921	0.045	0.033	5.05	0.32	664	33	573	101	690	10
B139.11	118	37	0.31	0.00011	0.0349	2.89	0.20	0.0637	0.001	0.108	0.002	0.948	0.024	0.033	3.14	0.61	664	21	731	42	661	10
B139.12	161	43	0.27	0.00007	0.0359	2.71	0.13	0.0634	0.001	0.110	0.002	0.961	0.022	0.035	3.04	0.64	692	21	722	37	672	9
B139.13	134	52	0.39	0.00038	0.0344	2.62	0.68	0.0591	0.001	0.111	0.002	0.904	0.025	0.030	3.21	0.55	606	19	571	51	678	10
B139.14	120	59	0.49	0.00016	0.0354	2.49	0.28	0.0622	0.002	0.109	0.002	0.937	0.030	0.034	3.22	0.49	677	22	681	59	668	10
B139.15	65	18	0.28	0.00032	0.0342	3.94	0.56	0.0591	0.002	0.112	0.002	0.912	0.040	0.029	7.19	0.41	588	42	571	87	684	12
B139.16	100	31	0.31	0.00044	0.0355	3.10	0.77	0.0564	0.002	0.112	0.002	0.869	0.038	0.030	6.49	0.37	594	39	470	90	682	10
B139.17**	98	45	0.45	0.00123	0.0355	3.11	2.17	0.0582	0.006	0.101	0.002	0.812	0.080	0.025	11.34	0.17	507	57	537	212	622	10
B139.18	156	41	0.27	0.00000	0.0371	2.69	0.00	0.0645	0.001	0.113	0.002	1.005	0.022	0.037	2.65	0.67	737	20	757	33	691	9
B139.19**	72	24	0.34	0.00014	0.0386	4.61	0.25	0.063	0.004	0.112	0.002	0.973	0.072	0.037	9.80	0.25	732	72	709	151	684	12
B139.20	69	22	0.32	0.00048	0.0355	3.60	0.85	0.0603	0.002	0.109	0.002	0.903	0.029	0.030	3.68	0.55	588	22	614	58	665	11
B139.21	130	64	0.49	0.00043	0.0323	2.47	0.77	0.0582	0.003	0.107	0.002	0.857	0.044	0.029	5.46	0.30	576	31	536	107	654	10
Sample B-mine (Bulgah quartz diorite)																						
B-mine.1	58	16	0.28	0.00046	0.0374	3.68	0.54	0.0598	3.888	0.111	1.539	0.911	4.182	0.031	6.61	0.37	610	40	596	84	676	10
B-mine.2**	60	16	0.27	0.00059	0.0460	7.80	0.46	0.0595	7.185	0.123	2.005	1.006	7.460	0.036	10.10	0.27	719	73	586	156	746	14
B-mine.3	75	32	0.43	0.00028	0.0343	2.96	0.48	0.0615	2.817	0.108	1.453	0.919	3.169	0.032	3.52	0.46	631	22	657	60	663	9
B-mine.4	69	22	0.32	0.00033	0.0386	3.22	0.68	0.0627	6.80	0.110	1.537	0.951	6.968	0.034	10.36	0.22	685	71	700	145	673	10
B-mine.5	102	35	0.35	0.00035	0.0352	3.03	0.39	0.0603	4.30	0.111	1.346	0.921	4.506	0.031	6.55	0.30	620	41	615	93	677	9
B-mine.6	70	21	0.30	0.00041	0.0349	3.33	0.67	0.0610	5.03	0.107	1.484	0.899	5.243	0.030	8.79	0.28	588	52	638	108	655	9
B-mine.7	76	21	0.28	0.00047	0.0349	3.32	0.46	0.0584	5.42	0.107	1.462	0.861	5.617	0.028	10.00	0.26	565	57	546	118	655	9
B-mine.8	74	28	0.37	0.00027	0.0351	3.29	0.31	0.0605	3.23	0.109	1.433	0.909	3.532	0.032	4.50	0.41	641	29	620	70	667	9
B-mine.9	163	58	0.36	0.00019	0.0338	2.25	0.04	0.0592	2.66	0.108	1.190	0.879	2.916	0.032	3.75	0.41	629	24	573	58	660	7

(continued)

Table 6.1 (continued)

Spot No.	U ppm	Th ppm	Th/U	$^{204}Pb/$ ^{206}Pb	$^{208}Pb/$ ^{232}Th	% error	$f206$ %	$^{207}Pb*/$ $^{206}Pb*$	% error	$^{206}Pb*/$ ^{238}U	% error	$^{207}Pb*/$ ^{235}U	% error	$^{208}Pb/$ ^{232}Th	% error	err corr	AGE 204 correction $^{208}Pb/$ ^{232}Th	1σ error	$^{207}Pb*/$ $^{206}Pb*$	1σ error	$^{206}Pb*/$ ^{238}U	1σ error
B-mine.10	150	61.1	0.41	0.00019	0.0346	2.20	0.07	0.0597	2.84	0.109	1.213	0.902	3.088	0.033	3.58	0.39	651	23	594	62	670	8
Sample Hm19 (Humaymah diorite)																						
Hm19.1	76	27	0.36	0.00157	0.0467	2.26	2.77	0.0576	0.006	0.108	0.002	0.856	0.084	0.029	13.08	0.14	581	76	515	212	659	9
HM19.2	150	36	0.24	0.00008	0.0339	2.10	0.15	0.0638	0.001	0.112	0.001	0.986	0.021	0.035	3.144	0.52	702	22	736	38	685	7
Hm19.3*	188	67	0.36	0.00002	0.0333	1.75	0.04	0.0630	0.001	0.106	0.001	0.920	0.014	0.034	1.752	0.69	667	12	707	24	649	6
Hm19.4	106	29	0.28	0.00010	0.0362	2.33	0.18	0.0620	0.002	0.111	0.001	0.953	0.027	0.035	4.515	0.42	690	31	673	55	681	8
Hm19.5	325	124	0.38	0.00023	0.0366	1.39	0.41	0.0621	0.001	0.112	0.001	0.956	0.024	0.034	2.192	0.38	677	15	677	50	683	6
Hm19.6	232	113	0.49	0.00014	0.0338	1.49	0.25	0.0615	0.001	0.109	0.001	0.926	0.016	0.033	1.839	0.57	650	12	657	31	668	6
Hm19.7	100	30	0.30	0.00015	0.0366	2.28	0.27	0.0591	0.002	0.113	0.001	0.917	0.030	0.034	4.848	0.36	685	33	570	67	688	8
Hm19.8	138	57	0.41	0.00033	0.0356	1.86	0.57	0.0590	0.001	0.111	0.001	0.905	0.024	0.032	3.013	0.42	644	19	568	51	679	7
Hm19.9	149	44	0.30	0.00005	0.0344	2.12	0.10	0.0607	0.001	0.108	0.001	0.906	0.024	0.034	3.857	0.41	669	26	629	52	662	7
Hm19.10	86	23	0.27	0.00035	0.0354	2.55	0.62	0.0596	0.002	0.113	0.001	0.926	0.037	0.03	7.503	0.31	596	45	589	81	688	8
Hm19.11	96	34	0.36	0.00070	0.0363	2.63	1.23	0.0556	0.003	0.107	0.001	0.821	0.046	0.029	7.342	0.23	569	42	437	121	656	8
Hm19.12	139	38	0.27	0.00140	0.0465	2.80	2.47	0.0562	0.005	0.109	0.001	0.841	0.082	0.026	18.6	0.13	516	96	459	215	664	8
Hm19.13	104	36	0.35	0.00001	0.0365	3.15	0.02	0.0644	0.001	0.112	0.001	0.994	0.019	0.037	2.165	0.63	727	16	753	31	685	8
Hm19.14	138	57	0.42	0.00005	0.0354	2.01	0.09	0.0616	0.001	0.113	0.001	0.956	0.021	0.035	2.61	0.51	693	18	660	40	688	7
Hm19.15	101	36	0.36	0.00020	0.0357	2.16	0.35	0.0617	0.002	0.112	0.002	0.954	0.031	0.034	4.419	0.37	666	29	665	66	685	8
Hm19.16*	240	75	0.31	0.00003	0.0361	1.67	0.05	0.0634	0.001	0.109	0.001	0.949	0.015	0.036	2.104	0.61	711	15	721	27	664	6
Hm19.17	177	86	0.49	0.00001	0.0355	1.68	0.01	0.0638	0.001	0.112	0.001	0.985	0.019	0.035	1.731	0.61	704	12	736	33	684	8
Hm19.18*	112	24	0.22	0.00247	0.0617	12.82	4.34	0.0437	0.019	0.115	0.003	0.69	0.297	0.000	0.000	0.05	0	0	-129	1064	699	16
Hm19.19	76	23	0.31	0.00025	0.0356	2.79	0.45	0.0679	0.003	0.112	0.002	1.047	0.043	0.039	6.067	0.42	772	47	865	77	683	11
Hm19.20	110	33	0.30	0.00011	0.0370	2.24	0.19	0.0628	0.002	0.112	0.001	0.972	0.032	0.036	4.054	0.36	707	29	702	65	686	8
Hm19.21	95	28	0.29	0.00014	0.0354	2.33	0.25	0.0656	0.001	0.108	0.001	0.978	0.024	0.037	3.448	0.47	740	26	794	46	662	7

*Common lead corrected using the measured ^{204}Pb
**Indicates data excluded from calculated age

Table 6.2 LA-ICP-MS isotopic data for zircons from Saudi Arabia

| Spot | U | ^{206}Pb | Isotope ratios | | | | | | | | | Disc. | Min. rim | Ages | | | | | |
	ppm	ppm	^{206}Pb/^{204}Pb	^{207}Pb/^{206}Pb*	1σ	^{207}Pb/^{235}U*	1σ	^{206}Pb/^{238}U*	1σ	Rhô	(%)**	(%)***	^{207}Pb/^{206}Pb	1σ	^{207}Pb/^{235}U	1σ	^{206}Pb/^{238}U	1σ
Humaymah tonalite (HC196, n = 14)																		
HC196-01	238	23	7960	0.061600	0.000480	0.870350	0.012180	0.102467	0.001189	0.83	2.5	0	653	17	641	7	638	8
HC196-02*	149	14	3585	0.061060	0.000480	0.877320	0.012320	0.104203	0.001211	0.83	5	0	660	16	636	7	629	7
HC196-03	169	16	3553	0.060760	0.000490	0.878010	0.012490	0.104802	0.001223	0.82	0.4	0	641	15	640	7	639	7
HC196-05	179	17	5076	0.061530	0.000500	0.895960	0.012740	0.105612	0.001235	0.82	1.9	0	631	16	640	7	642	7
HC196-06	149	14	4985	0.061080	0.000500	0.889420	0.012840	0.105618	0.001257	0.83	1.7	0	658	16	650	7	647	7
HC196-07	230	22	6911	0.061430	0.000520	0.887330	0.013220	0.104755	0.001278	0.82	0.9	0	642	17	646	7	647	7
HC196-08*	236	21	5802	0.062440	0.000500	0.840990	0.012380	0.097679	0.001211	0.84	13.5	8.2	689	16	620	7	601	7
HC196-09	154	15	4620	0.061470	0.000560	0.879320	0.013230	0.103747	0.001236	0.79	2	0.0	654	17	645	7	642	7
HC196-11	128	12	3809	0.062260	0.000560	0.897630	0.013480	0.104570	0.001261	0.80	3.1	0.0	656	19	641	7	636	7
HC196-12	101	10	3249	0.060700	0.000490	0.884230	0.012800	0.105650	0.001271	0.83	6.4	0.1	683	18	650	7	641	7
HC196-13	210	20	4786	0.061350	0.000510	0.891900	0.013010	0.105438	0.001267	0.82	3.1	0	629	17	643	7	647	7
HC196-14	163	16	5591	0.061100	0.000490	0.884830	0.012920	0.105026	0.001283	0.84	0.9	0	652	17	647	7	646	7
HC196-17	256	24	9562	0.061430	0.000520	0.884190	0.013160	0.104383	0.001272	0.82	0.2	0	643	17	644	7	644	7
HC196-18	135	13	4827	0.061400	0.000500	0.880050	0.012990	0.103955	0.001285	0.84	2.3	0	655	18	643	7	640	7

*Indicated data excluded from calculated age
**Discordance from the centre of an error ellipse
***Minimum discordance from the rim of an error ellipse

Table 6.3 Major and trace elements of the intrusive rocks from Saudi Arabia

Sample	DL	B20	B21	B22	B24	B26	B27	B28	B29	B30	B31	B32	B39	B40
SiO_2	0.01	51.4	54.7	54.1	56.0	68.1	69.3	68.2	67.4	66.9	68.0	66.4	64.6	65.4
TiO_2	0.01	0.74	0.78	0.77	0.79	0.36	0.33	0.37	0.35	0.35	0.31	0.51	0.5	0.4
Al_2O_3	0.01	17.4	16.2	17.95	16.55	15.15	14.95	15.1	15	14.95	14.65	15.25	14.15	13.7
Fe_2O_3	0.04	7.28	7.21	7.41	6.55	2.8	2.63	2.69	2.73	2.82	2.52	4.03	3.96	3.28
MnO	0.01	0.14	0.14	0.13	0.13	0.04	0.03	0.04	0.04	0.05	0.05	0.04	0.05	0.05
MgO	0.01	1.7	1.87	2.28	1.41	1.41	1.37	1.5	1.57	1.53	1.35	2.23	2.08	1.98
CaO	0.01	7.31	6.81	6.35	6.3	2.83	2.21	3.04	2.99	3.76	3.33	1.99	4.81	4.56
Na_2O	0.01	4.79	3.23	4.41	5.19	4.26	4.71	4.9	4.24	4.31	4.69	4.97	3.1	3.98
K_2O	0.01	2.61	3.51	1.94	2.94	3.12	3.07	2.6	2.52	2.41	2.83	2.39	2.98	2.81
P_2O_5	0.01	0.42	0.43	0.42	0.5	0.11	0.12	0.12	0.11	0.12	0.1	0.14	0.14	0.15
LOI	0.1	4.6	4.5	4.6	4.5	3.2	2.6	3.1	3.6	3.8	3.3	2.8	4.4	4.2
Total		98.5	99.5	100.5	101.0	101.5	101.4	101.8	100.6	101.1	101.3	101.0	100.9	100.7
Ni	20	5	9	7	4	15	14	14	14	14	12	20	19	36
Cr	2	20	30	20	20	80	70	70	70	70	60	70	70	130
Co	20	16	17	19	15	6	7	7	7	9	6	11	12	10
Sc	1	14	13	12	9	2	2	2	1	1	1	4	4	3
V	8	197	165	192	151	53	49	54	55	52	51	83	89	65
Cu	5	195	166	205	163	25	28	23	16	12	24	24	31	26
Ag	0.1	0.2	bdl	bdl	bdl	bdl	bdl	bdl	0.4	0.5	0.3	bdl	0.3	bdl
Pb	1	19	10	10	13	9	6	7	7	294	34	10	5	7
Zn	5	141	91	114	95	27	24	24	131	57	23	32	33	30
Sn	1	1	1	1	1	1	1	1	1	1	1	1	1	1
Ba	1	10	20	30	10	40	30	30	30	30	100	650	40	40
Rb	0.1	46.1	70.1	39.7	47.3	85.5	73.7	63.4	81.4	76.4	72.8	55.8	88.9	64.7
Cs	0.1	1.4	2.3	2.5	1.2	1.5	1.1	1.1	1.2	1.0	1.2	1.0	1.8	1.1
Sr	0.5	618	430	636	422	499	495	549	421	420	430	464	424	468
Ga	0.5	21.2	18.3	20	17.7	18	17.9	18	18.1	18.1	17.8	18.4	17.2	17
Hf	0.1	3.2	3.5	3.3	3.7	3.2	3.7	3.3	3	2.9	3.2	3	3.2	3.3
Nb	0.1	6.9	7.7	6.9	8.1	4.3	7.3	4.8	4.3	4.3	4.1	4	3.4	4.4
Zr	5	117	129	119	141	133	139	135	123	122	131	116	114	117
Y	3	26	26	25	28	11	11	9	9	9	11	14	11	14
Ta	0.1	0.5	0.5	0.5	0.5	0.3	0.4	0.3	0.3	0.4	0.3	0.3	0.2	0.4
Th	0.2	2.5	2.7	2.4	2.9	5.5	9.0	6.6	5.0	4.7	7.2	8.1	5.5	9.6
U	0.1	0.8	0.9	0.8	1.0	3.3	4.2	3.6	3.1	3.0	4.0	3.9	3.3	5.0

(continued)

Table 6.3 (continued)

Sample	DL	B20	B21	B22	B24	B26	B27	B28	B29	B30	B31	B32	B39	B40
La	0.1	15.7	14.2	12.9	15.5	13.4	17.8	15.2	12	13.9	15.7	17.3	13.5	14.8
Ce	0.1	33.0	31.9	29.5	35.5	26.1	33.3	28.6	23.7	25.8	28.0	31.1	26.7	28.2
Pr	0.02	4.33	4.24	3.93	4.76	3.08	3.82	3.28	2.82	2.89	3.13	3.6	3.22	3.25
Nd	0.3	19.7	18.6	17.9	20.7	11.6	14.1	12.6	10.2	10.7	12.1	14.9	12.0	12.1
Sm	0.05	4.62	5.15	4.59	5.25	2.13	2.88	2.39	2.19	1.99	2.37	3.25	2.57	2.51
Eu	0.02	1.47	1.26	1.20	1.27	0.56	0.71	0.65	0.57	0.52	0.59	0.67	0.87	0.91
Gd	0.05	4.50	4.60	4.63	5.12	1.89	2.36	1.98	1.70	1.81	2.14	2.97	2.50	2.66
Tb	0.01	0.72	0.74	0.74	0.83	0.31	0.35	0.28	0.28	0.29	0.34	0.46	0.39	0.4
Dy	0.05	4.40	4.37	4.46	4.98	1.66	2.09	1.61	1.60	1.62	1.94	2.67	2.17	2.52
Ho	0.02	0.96	0.94	0.94	1.05	0.33	0.40	0.34	0.33	0.30	0.39	0.51	0.43	0.52
Er	0.03	2.79	2.77	2.76	3.07	0.93	1.09	0.86	0.84	0.86	1.17	1.33	1.22	1.44
Tm	0.01	0.40	0.40	0.43	0.47	0.15	0.17	0.12	0.15	0.13	0.15	0.21	0.17	0.21
Yb	0.05	2.68	2.85	2.53	2.87	0.93	0.85	0.81	0.84	0.84	0.98	1.16	1.09	1.36
Lu	0.01	0.43	0.45	0.42	0.52	0.14	0.17	0.14	0.14	0.12	0.16	0.17	0.18	0.18
Eu/Eu*		0.98	0.79	0.79	0.75	0.85	0.83	0.91	0.90	0.84	0.80	0.66	1.05	1.08
K/Rb		0.001	0.001	0.001	0.001	0.001	0.001	0.001	0.001	0.001	0.001	0.001	0.001	0.001
Mg#		45.3	46.9	45.0	44.0	26.8	25.8	26.1	26.5	27.2	25.4	34.4	35.7	32.2
Al		0.62	0.56	0.52	0.71	0.69	0.74	0.72	0.65	0.65	0.74	0.71	0.59	0.70
La/Nb		2.3	1.8	1.9	1.9	3.1	2.4	3.2	2.8	3.2	3.8	4.3	4.0	3.4
(La/Yb)N		3.98	3.38	3.46	3.67	9.79	14.23	12.75	9.70	11.24	10.88	10.13	8.41	7.39
(Dy/Yb)N		1.07	1.00	1.15	1.14	1.17	1.61	1.30	1.25	1.26	1.30	1.51	1.30	1.21
(Y/Nb)N		0.58	0.53	0.56	0.55	0.39	0.23	0.30	0.33	0.33	0.43	0.54	0.51	0.48
(Th/Nb)N		3.01	2.92	3.00	3.05	10.79	10.42	11.66	9.90	9.29	14.86	17.26	13.70	18.43
(Th/Ta)N		2.37	2.56	2.36	2.81	8.80	10.83	10.62	8.08	5.68	11.55	13.10	13.25	11.54
(Ce/Pb)N		0.07	0.13	0.12	0.11	0.12	0.22	0.16	0.01	0.00	0.03	0.12	0.21	0.16

(continued)

Table 6.3 (continued)

Sample	B41	B42	B43	B44	B45	B46	B48	B49	B50	B53	B54	B11	B14
SiO_2	67.4	69.2	67.9	67.1	67.1	74.7	72.5	74.3	74.5	70.5	72.7	55.1	57.5
TiO_2	0.38	0.3	0.33	0.35	0.31	0.19	0.24	0.18	0.19	0.23	0.24	0.98	0.99
Al_2O_3	14.4	14.25	14.25	14.35	13.8	13.00	13.95	12.95	13.00	13.60	13.95	14.63	16.74
Fe_2O_3	2.94	2.39	2.46	2.69	2.26	2.34	2.7	2.32	2.32	2.6	2.55	7.16	6.28
MnO	0.05	0.03	0.03	0.04	0.04	0.05	0.06	0.05	0.05	0.05	0.06	0.1	0.09
MgO	1.78	1.32	1.32	1.18	1.06	0.30	0.63	0.30	0.30	0.61	0.62	6.5	3.59
CaO	3.5	2.69	2.63	3.07	3.7	1.06	1.73	1.05	1.06	1.68	1.72	6.83	4.53
Na_2O	4.57	4.2	4.17	5.33	5.31	4.53	4.10	4.51	4.55	4.02	4.12	3.85	4.31
K_2O	2.27	2.88	2.79	2.45	2.33	4.11	3.51	4.08	4.11	3.43	3.52	2.49	3.16
P_2O_5	0.12	0.11	0.11	0.12	0.13	0.05	0.09	0.04	0.06	0.08	0.09	0.27	0.29
LOI	3.4	2.7	2.8	2.9	3.4	0.93	1.14	0.91	0.87	1.13	1.13	1.7	2.3
Total	101.0	100.2	98.9	99.7	99.5	101.4	100.8	100.8	101.1	98.1	100.9	99.65	99.73
Ni	24	13	15	14	13	1	3	1	2	3	3	123	57
Cr	100	70	70	60	60	20	20	20	10	30	40		
Co	8	5	6	7	6	2	3	2	1	3	3	29.9	18.9
Sc	3	2	2	3	2	3	2	3	3	2	2	20	14
V	58	52	52	47	47	13	24	15	12	23	23	147	120
Cu	16	16	24	27	23	7	5	7	7	5	5	42.1	19.6
Ag	bdl	bdl	bdl	bdl	bdl	bdl	bdl	bdl	bdl	bdl	bdl	0.1	0.1
Pb	4	5	8	6	7	24	4	24	23	4	3	5	4.7
Zn	32	23	23	22	20	68	45	66	67	43	41	27	35
Sn	1	1	1	1	1	4	3	4	4	3	3	2	1
Ba	30	20	20	40	30	110	120	110	110	120	110	538	592
Rb	54.7	82.8	78.8	57.9	58.9	101.0	93.8	106.5	105.0	90.6	94.8	53.5	66.5
Cs	1.0	1.2	1.3	0.7	0.7	1.1	0.8	1.1	1.2	0.9	0.9	1.7	0.9
Sr	620	549	477	377	300	110.5	431	119.5	115	405	423	640	931
Ga	17.4	18.6	17.1	16.7	16.4	19.6	18.2	21.6	20.5	16.8	16.8	16.6	18.2
Hf	3	3.2	3.4	3.5	4	7.6	3.9	8.1	7.6	3.5	4.1	4.1	4.5
Nb	3.9	3.9	3.6	3.8	3.8	9.5	6.7	10	9.7	6.5	6.8	7.5	7.7
Zr	118	125	129	130	147	272	166	280	258	134	153	159	159
Y	8	8	7	19	24	36	8	39	37	7	7	16	15
Ta	0.3	0.3	0.2	0.2	0.3	0.7	0.5	0.7	0.7	0.5	0.5	0.4	0.5
Th	4.8	5.9	4.8	14.7	20.0	10.6	7.5	11.3	10.7	7.4	7.6	3.3	3.8
U	3.2	3.9	3.2	5.7	9.6	3.4	3.7	3.7	3.6	3.7	3.7	1.8	2.0

(continued)

Table 6.3 (continued)

Sample	B41	B42	B43	B44	B45	B46	B48	B49	B50	B53	B54	B11	B14
La	13.6	15.2	13	13.7	16.2	39.2	22.8	43.9	39	23	24.1	15.3	18.3
Ce	25.6	28.1	24.8	27.0	30.8	81.6	40.6	91.2	81.4	40.6	42.7	33.6	37.1
Pr	3.07	3.08	2.82	3.34	3.84	9.64	4.27	10.75	9.64	4.21	4.41	4.57	4.85
Nd	11.2	11.5	10.8	13.5	15.8	37.1	14.8	41.0	36.8	14.3	14.9	18.5	18.4
Sm	1.91	2.21	1.75	3.35	4.30	6.96	2.23	7.97	7.45	2.26	2.49	3.77	3.64
Eu	0.75	0.58	0.62	0.88	1.02	0.85	0.54	0.87	0.83	0.49	0.57	1.18	1.15
Gd	1.75	2.03	1.73	3.84	5.15	6.47	1.71	7.26	6.25	1.68	1.74	3.55	3.37
Tb	0.26	0.25	0.26	0.66	0.84	1.05	0.23	1.09	1.06	0.23	0.26	0.55	0.54
Dy	1.31	1.27	1.37	3.87	5.01	6.4	1.4	7.2	6.7	1.2	1.4	2.82	2.73
Ho	0.27	0.26	0.24	0.79	0.94	1.42	0.26	1.45	1.31	0.27	0.26	0.56	0.54
Er	0.74	0.74	0.66	1.97	2.33	4.05	0.74	4.5	4.17	0.72	0.77	1.7	1.57
Tm	0.11	0.12	0.11	0.23	0.30	0.6	0.11	0.68	0.61	0.1	0.1	0.24	0.25
Yb	0.82	0.65	0.70	1.52	1.54	4.18	0.78	4.33	4.15	0.72	0.82	1.43	1.43
Lu	0.12	0.12	0.11	0.18	0.21	0.65	0.12	0.66	0.66	0.12	0.1	0.22	0.21
Eu/Eu*	1.25	0.84	1.09	0.75	0.66	0.39	0.84	0.35	0.37	0.77	0.84	0.98	1.00
K/Rb	0.001	0.001	0.001	0.001	0.001	0.001	0.001	0.001	0.001	0.001	0.001	0.001	0.001
Mg#	28.8	24.9	25.5	27.1	24.5	26.3	27.7	26.2	26.1	27.5	26.6	49.2	42.6
Al	0.69	0.70	0.69	0.80	0.82	0.92	0.76	0.91	0.92	0.76	0.76	0.62	0.63
La/Nb	3.5	3.9	3.6	3.6	4.3	4.1	3.4	4.4	4.0	3.5	3.5	2.0	2.4
(La/Yb)N	11.27	15.89	12.62	6.12	7.15	6.37	19.86	6.89	6.38	21.70	19.97	7.27	8.69
(Dy/Yb)N	1.05	1.28	1.28	1.67	2.13	1.00	1.16	1.09	1.05	1.13	1.13	1.29	1.25
(Y/Nb)N	0.31	0.31	0.31	0.80	0.99	0.60	0.18	0.62	0.59	0.17	0.17	0.33	0.31
(Th/Nb)N	10.48	12.85	11.38	32.81	44.65	9.46	9.46	9.59	9.31	9.66	9.43	3.73	4.19
(Th/Ta)N	7.76	9.51	11.66	35.48	32.18	7.31	7.21	7.79	7.34	7.14	7.30	3.98	3.67
(Ce/Pb)N	0.26	0.22	0.12	0.18	0.18	0.14	0.41	0.15	0.14	0.41	0.57	0.27	0.32

(continued)

Table 6.3 (continued)

Sample	B139	C57	C58	B12	B13	Bulc	Bul	C55	HUM1	HUM2	HUM3	HUM4	HUM1A
Sample	B139	C57	C58	B12	B13	Bulc	Bul	C55	HUM1	HUM2	HUM3	HUM4	HUM1A
SiO_2	54.6	58.4	58.5	65.9	69.3	66.5	73.5	71.1	49.9	52.4	55.0	54.7	49.4
TiO_2	0.9	1.02	0.99	0.47	0.37	0.41	0.21	0.28	1.3	0.82	1.17	1.12	1.3
Al_2O_3	19.95	16.07	16.67	14.83	15.4	15.88	12.39	13.57	15.4	14.0	16.5	16.3	15.6
Fe_2O_3	2.22	5.83	5.89	3.59	2.72	3.08	1.06	2.39	9.89	9.63	8.66	9.19	9.71
MnO	0.05	0.08	0.09	0.04	0.04	0.04	0.03	0.06	0.17	0.17	0.15	0.15	0.17
MgO	2.16	3.34	3.6	2.33	1.42	1.91	0.3	1.05	7.85	8.91	4.89	5.28	7.78
CaO	9.95	4.28	4.78	2.67	1.17	2.9	2.66	2.2	10.30	10.00	8.04	8.47	10.15
Na_2O	5.85	5.43	4.18	3.91	4.84	5.19	3.91	3.8	2.30	1.80	3.09	2.82	2.32
K_2O	1.07	2.92	2.7	2.89	2.57	1.49	2.79	4.03	0.39	0.40	1.07	0.78	0.39
P_2O_5	0.25	0.29	0.27	0.15	0.14	0.14	0.04	0.06	0.16	0.14	0.30	0.20	0.16
LOI	2.8	2.1	2	3	1.9	2.2	2.9	1.2	0.99	1.23	1.34	1.23	1.03
Total	99.75	99.77	99.68	99.8	99.88	99.72	99.82	99.75	98.8	99.6	100.3	100.3	98.1
Ni	20	30	26	28	20	26	20	20	19	30	12	19	16
Cr									370	610	140	140	320
Co	5	20.6	23.6	9.8	6.5	9.1	8.6	15.6	15	16	13	19	14
Sc	10	14	14	7	5	6	3	5	3	3	2	3	3
V	83	140	132	57	38	51	11	30	301	267	181	232	252
Cu	35.8	23.8	16.8	17	14.2	12.3	5.6	4.9	9	11	14	16	9
Ag	0.1	0.1	0.1	0.1	0.1	0.1	0.1	0.1	bdl	bdl	bdl	bdl	bdl
Pb	6.8	9	6	5.6	10.6	3.6	7	11	2	bdl	2	bdl	2
Zn	28	47	40	39	54	45	31	41	21	17	36	28	19
Sn	4	1	2	1	1	1	2	1	<1	1	1	1	<1
Ba	92	329	584	570	576	482	502	1015	30	20	50	30	30
Rb	42.5	61	62	75.8	67.3	40	60	63	6.6	8.2	24.5	18.2	5.7
Cs	1.5	1.4	1.3	2.8	1.4	1.2	1.0	0.5	0.4	0.7	0.8	1.0	0.4
Sr	868	290	987	483	502	887	204	250	415	371	451	443	409
Ga	14.5	17.1	18.3	16.1	14.7	17.1	12.9	13.4	16.8	15.1	19.1	18.3	16.5
Hf	6.7	5	4.2	3.5	3.5	3.4	4.9	4.2	1.3	0.8	2.4	2.8	1.1
Nb	10.2	7.8	7.9	4.9	4.2	4.5	6.1	5.7	6.9	3.9	13.5	7.4	8.3
Zr	268	171	161	128	120	131	175	138	43	29	104	114	38
Y	18	15	15	8	7	7	16	13	14	11	17	17	14
Ta	0.7	0.6	0.6	0.3	0.2	0.3	0.8	0.5	0.4	0.2	0.8	0.5	0.2
Th	6.5	4.2	3.9	4.8	4.8	3.3	9.4	10.4	0.2	0.2	2.3	1.1	0.2
U	3.2	2.0	2.0	2.6	2.3	2.2	5.0	3.0	0.2	0.1	1.0	0.6	0.1
La	16	19.3	19.2	14.2	16.5	12.6	24.1	21.4	6.1	4.3	15.6	9.1	6.2

Table 6.3 (continued)

Sample	B139	C57	C58	B12	B13	Bulc	Bul	C55	HUM1	HUM2	HUM3	HUM4	HUM1A
Ce	36.3	39.4	40.3	28.5	28.5	25.8	50.5	42.9	13.6	9.5	30.5	20.4	13.2
Pr	5.02	5.1	5	3.51	3.38	3.07	5.1	4.3	1.89	1.32	3.73	2.78	1.86
Nd	19.5	19.4	18.9	13.4	12.7	11.3	18.8	16.0	8.8	6.6	15.6	12.1	9.2
Sm	4.3	3.79	3.7	2.25	2.22	2.17	3.36	2.8	2.36	1.70	3.50	2.99	2.72
Eu	1.34	1.14	1.16	0.67	0.68	0.71	0.62	0.47	0.98	0.91	1.25	1.11	1
Gd	3.95	3.55	3.41	2.04	1.94	1.82	2.89	2.36	2.87	2.21	3.47	3.27	2.84
Tb	0.61	0.53	0.53	0.29	0.27	0.26	0.44	0.36	0.45	0.36	0.56	0.51	0.46
Dy	3.11	2.81	2.79	1.37	1.29	1.35	2.56	2.13	2.8	2.1	3.1	3.4	2.5
Ho	0.66	0.57	0.56	0.3	0.25	0.26	0.51	0.45	0.59	0.41	0.66	0.67	0.53
Er	1.85	1.58	1.6	0.8	0.72	0.76	1.67	1.29	1.61	1.18	1.73	1.95	1.35
Tm	0.28	0.23	0.23	0.13	0.11	0.12	0.28	0.23	0.22	0.17	0.25	0.27	0.2
Yb	1.68	1.45	1.37	0.8	0.71	0.71	1.77	1.5	1.46	1.11	1.54	1.94	1.33
Lu	0.24	0.21	0.19	0.13	0.11	0.11	0.3	0.25	0.22	0.17	0.26	0.26	0.2
Eu/Eu*	0.99	0.95	1.00	0.95	1.00	1.09	0.61	0.56	1.15	1.43	1.10	1.08	1.10
K/Rb	0.001	0.001	0.001	0.001	0.001	0.001	0.001	0.001	0.001	0.001	0.001	0.001	0.001
Mg#	18.1	41.8	41.2	32.4	25.9	27.8	14.5	25.9	56.0	57.7	51.0	52.8	55.3
Al	0.54	0.75	0.59	0.64	0.70	0.64	0.76	0.78	0.27	0.24	0.38	0.34	0.27
La/Nb	1.6	2.5	2.4	2.9	3.9	2.8	4.0	3.8	0.9	1.1	1.2	1.2	0.7
(La/Yb)N	6.47	9.04	9.52	12.06	15.79	12.06	9.25	9.69	2.84	2.63	6.88	3.19	3.17
(Dy/Yb)N	1.21	1.27	1.33	1.12	1.19	1.24	0.95	0.93	1.24	1.25	1.31	1.14	1.24
(Y/Nb)N	0.27	0.31	0.30	0.26	0.26	0.26	0.42	0.34	0.33	0.44	0.19	0.36	0.25
(Th/Nb)N	5.41	4.57	4.19	8.31	9.69	6.22	13.07	15.48	0.26	0.52	1.43	1.28	0.17
(Th/Ta)N	4.48	3.38	3.14	7.72	11.59	5.31	5.67	10.04	0.25	0.58	1.37	1.08	0.41
(Ce/Pb)N	0.21	0.18	0.27	0.20	0.11	0.29	0.29	0.16	0.27	0.19	0.61	0.41	0.26

(continued)

Table 6.3 (continued)

Sample	HUM1B	HUM2A	HUM2B	HUM3A	HUM3B	HUM4A	HUM4B	Hm2	HM20	HM18	HM19	C47	C48
SiO_2	50.1	52.6	52.6	54.6	54.5	53.9	54.4	50.3	49.3	49.0	64.3	52.4	54.5
TiO_2	1.32	0.83	0.84	1.15	1.16	1.14	1.14	1.59	1.6	0.45	0.65	0.77	1.48
Al_2O_3	15.7	14.3	14.4	16.8	16.8	16.4	16.5	19.33	18.2	15.37	15.78	15.55	15.86
Fe_2O_3	9.88	9.63	9.61	8.52	8.47	9.00	9.12	9.12	9.62	8.57	5.35	9.09	8.7
MnO	0.17	0.17	0.17	0.15	0.15	0.15	0.15	0.11	0.16	0.15	0.05	0.15	0.13
MgO	7.88	8.99	8.98	4.86	4.83	5.22	5.27	3.95	6.36	10.64	1.78	7.2	4.11
CaO	10.25	9.96	9.96	7.92	7.86	8.25	8.32	9.71	10.04	12.22	4.26	7.27	5.82
Na_2O	2.35	1.85	1.86	3.16	3.14	2.85	2.87	3.97	2.7	1.05	4.09	3.27	3.54
K_2O	0.39	0.41	0.41	1.07	1.07	0.77	0.77	0.29	0.44	0.43	0.89	1.53	2.5
P_2O_5	0.16	0.13	0.14	0.30	0.30	0.20	0.21	0.62	0.39	0.04	0.16	0.23	0.38
LOI	0.96	1.17	1.42	1.35	1.29	1.24	1.22	0.7	0.9	1.7	2.5	2.1	2.6
Total	99.3	100.2	100.5	99.9	99.6	99.2	100.0	99.7	99.8	99.7	99.9	99.5	99.6
Ni	17	30	29	12	10	19	19	53	21	62	20	123	28
Cr	330	530	530	120	130	120	120						
Co	13	16	15	12	12	18	19	48	32.7	38.3	11.1	36.1	30.3
Sc	3	2	2	2	2	3	3	20	26	39	9	21	16
V	259	228	224	154	158	194	200	165	243	296	64	201	158
Cu	9	10	10	14	13	15	16	151.3	19.4	4.7	34.9	39.7	16.2
Ag	bdl	bdl	bdl	bdl	bdl	bdl	bdl	0.1	0.1	0.1	0.1	0.1	0.1
Pb	3	2	bdl	bdl	bdl	2	2	1	3	11	4	7	4
Zn	19	16	16	33	32	27	28	29	22	14	46	44	85
Sn	<1	1	1	1	1	1	1	<1	1	1	1	1	2
Ba	30	20	20	50	50	30	30	118	127	58	338	757	484
Rb	6.0	7.8	7.9	22.6	22.7	16.8	17.2	5.4	8.5	9.2	19.3	35	64.2
Cs	0.4	0.7	0.7	0.8	0.8	1.0	1.1	0.7	0.7	0.6	0.3	1.5	2.1
Sr	418	383	381	453	455	433	444	735	545	390	409	753	637
Ga	16.4	14.5	14.7	18.2	18.6	17.3	17.9	18.2	17.8	13.3	17.8	19.6	20
Hf	1.3	0.7	0.8	2.7	3.2	2.4	2.4	1.2	1.1	0.5	6.9	2.1	4.4
Nb	7.3	3.8	3.7	13.2	13.7	7.2	7.3	17	9.4	1.2	17.2	2.8	11.6
Zr	40	24	28	102	127	97	89	51	34	16	240	64	157
Y	14	10	10	16	16	16	17	14	13	9	20	10	25
Ta	0.2	<0.1	<0.1	0.6	0.6	0.3	0.3	1	0.5	0.1	0.9	0.3	0.9
Th	0.2	0.2	0.2	2.4	2.3	1.0	1.1	0.5	0.4	0.2	8.1	3.5	4.8
U	0.1	0.1	0.1	0.9	1.0	0.5	0.5	0.5	0.2	0.1	3.1	1.0	2.8

(continued)

Table 6.3 (continued)

Sample	HUM1B	HUM2A	HUM2B	HUM3A	HUM3B	HUM4A	HUM4B	Hm2	HM20	HM18	HM19	C47	C48
La	6.3	4.4	4.2	16	16.1	9.4	9.4	12.1	8.6	2.7	33.2	14.4	20.8
Ce	13.5	9.1	9.4	29.7	30.3	19.6	19.7	27.0	18.0	6.2	58.8	30.3	48.8
Pr	1.99	1.33	1.35	3.67	3.76	2.78	2.74	3.48	2.52	0.95	6.58	3.7	6.44
Nd	9.3	6.9	6.7	16.0	15.7	11.8	12.2	16.2	11.7	4.6	23.1	15.6	26.2
Sm	2.52	1.83	1.83	3.42	3.69	3.24	3.15	3.3	2.48	1.46	4.27	3.2	5.95
Eu	1.01	0.83	0.83	1.16	1.14	1.03	1.12	1.43	1.22	0.72	1.05	1.04	1.61
Gd	2.75	2.17	2.15	3.55	3.68	3.27	3.49	3.47	2.84	1.68	3.97	2.48	5.41
Tb	0.45	0.35	0.33	0.49	0.5	0.52	0.54	0.53	0.46	0.3	0.63	0.37	0.89
Dy	2.6	2.0	1.9	3.1	3.0	2.9	3.0	2.84	2.4	1.65	3.41	2	4.84
Ho	0.57	0.45	0.4	0.63	0.65	0.63	0.65	0.5	0.49	0.34	0.69	0.36	0.89
Er	1.34	1.04	1.08	1.62	1.66	1.63	1.62	1.42	1.33	0.94	2.02	1.02	2.5
Tm	0.2	0.17	0.18	0.25	0.24	0.24	0.26	0.19	0.2	0.16	0.29	0.14	0.36
Yb	1.44	1.04	1.08	1.65	1.49	1.63	1.69	1.14	1.25	0.89	1.83	0.87	2.19
Lu	0.21	0.16	0.16	0.23	0.23	0.26	0.25	0.17	0.18	0.14	0.29	0.14	0.33
Eu/Eu*	1.17	1.27	1.28	1.02	0.94	0.97	1.03	1.29	1.40	1.40	0.78	1.13	0.87
K/Rb	0.001	0.001	0.001	0.001	0.001	0.001	0.001	0.001	0.001	0.001	0.001	0.001	0.001
Mg#	55.5	57.2	57.0	50.2	50.0	52.2	52.3	48.3	51.2	52.5	40.2	53.7	52.1
Al	0.27	0.24	0.24	0.38	0.38	0.34	0.34	0.35	0.27	0.14	0.49	0.45	0.54
La/Nb	0.9	1.2	1.1	1.2	1.2	1.3	1.3	0.7	0.9	2.3	1.9	5.1	1.8
(La/Yb)N	2.97	2.87	2.64	6.59	7.34	3.92	3.78	7.21	4.67	2.06	12.32	11.24	6.45
(Dy/Yb)N	1.18	1.28	1.14	1.22	1.30	1.16	1.16	1.63	1.26	1.21	1.22	1.50	1.45
(Y/Nb)N	0.30	0.43	0.44	0.19	0.19	0.35	0.36	0.13	0.22	1.19	0.18	0.54	0.34
(Th/Nb)N	0.22	0.54	0.48	1.52	1.43	1.18	1.22	0.25	0.36	1.41	3.99	10.60	3.51
(Th/Ta)N	0.46	1.16	1.01	1.91	1.86	1.61	1.69	0.24	0.39	0.97	4.34	5.63	2.57
(Ce/Pb)N	0.18	0.18	0.19	0.59	0.61	0.39	0.39	1.08	0.29	0.02	0.60	0.17	0.48

Major (wt.%), trace and REE (ppm) elements were determined by ICP-AES (major elements) and ICP-MS (trace and REEs) at ACME Labs, Canada. Eu/Eu* = $Eu_N/SQRT(Sm_N \times Gd_N)$

Lithium borate fusion technique is used for all elements to completely decompose even most refractory matrices to provide total element concentrations. DL = detection limit and bdl = below detection limit. Major oxides detection limits in % and elements concentration detection limits in ppm

The volcanosedimentary rocks and intermediate to felsic intrusions of the Afif terrane were intruded by gabbros to highly evolved granites between $\sim$750 and 570 Ma. Based on their composition, textures and/or absolute ages, these rocks are classified from the oldest to the youngest as the Jidh, Suwaj, Fahud, Khishaybi, Humaymah, Haml and syn- to post-Shammar intrusions of the Idah and Abanat suites. The post-collision monzogranite rocks of Haml batholith were dated at 609 $\pm$ 8 Ma (Robinson et al. 2014).

6.3 Analytical Techniques

Four representative samples of the intrusive rocks were selected for dating using U–Pb zircon geochronology. Bulk samples of these rocks (each weight $\approx$ 3 kg) were crushed and pulverised to a fine fraction and sieved. The fractions of these samples that fall between 250 and +75 μm were washed by distilled water and dried. These initial sample preparations were carried out in the laboratory facilities at the department of Mineral Resources and Rocks at the Faculty of Earth Sciences, King Abdulaziz University (KAU) in Jeddah (Saudi Arabia). Heavy liquids were used to separate the heavy fraction from these samples using Methylene Iodide (specific gravity 3.3 gm/ml). The non-magnetic fraction of these samples which may contain the zircon grains were separated using a Franz Isodynamic separator. Finally, zircon grains were collected by hand-picking under a binocular stereoscopic microscope. Zircons were analysed for their U–Pb age at John de Laeter Centre, Curtin University of Technology (Australia) and at the University of Oslo (Norway).

Prior to analysis, zircon grains were imaged on the polished puck by cathodoluminecence (CL) to examine the growth structure of individual grains using a scanning electron microscope. U–Pb isotope data on zircons were obtained by laser-ablation inductively coupled plasma source mass spectrometry (LA-ICP-MS) using a Nu Plasma HR mass spectrometer and a New Wave LUV213 laser microprobe at University of Oslo (Norway) and by sensitive high resolution ion microprobe (SHRIMP II) at Curtin University (Australia). The analytical protocols of the LA-ICP-MS are described in detail by Rosa et al. (2009), and SHRIMP analytical procedure is described by Compston et al. (1984) and Kennedy and de Laeter (1994). The 1065 $\pm$ 0.6 Ma (2σ) Geostandards zircon 91500 (Wiedenbeck et al. 1995) and 600 $\pm$ 4.5 Ma (2σ) Geostandards GJ-1 (Jackson et al. 2004) were both used for Pb/U calibration and U concentration estimates and were analysed on a regular basis during the analytical sessions by LA-ICP-MS, and BR266 (559 Ma; 903 ppm U) was used for SHRIMP. Calculations used the routines of Isoplot

(Ludwig 2001a, b). U–Th–Pb concentrations and isotopic compositions are listed in Table 6.1 (SHRIMP II) and Table 6.2 (LA-ICP-MS), and plotted as two-sigma error ellipses on Concordia diagrams (Wetherill 1956).

A total of 53 intrusive samples were selected for major, trace and rare earth elements analyses. Major element compositions and Sc, Ba, and Ni abundances were determined by inductively coupled plasma-atomic emission spectrometry (ICP-AES). All the others trace and rare earth elements (REE) were determined by inductively coupled plasma-mass spectrometry (ICP-MS). All the analyses were carried out at the ACME Analytical Laboratories Ltd., Canada. Analytical precision, as calculated from replicate analyses, is 0.5% for major elements and varies from 2 to 20% for trace elements. Analytical results are listed in the Table 6.3.

6.4 Results

6.4.1 U–Pb Geochronology

Sample B139 (N25° 01′ 37.0″, E41° 36′ 32.9″) is a dark grey, coarse-grained diorite collected from Bulghah area. Zircons separated from this sample are euhedral, acicular, and yellowish brown in color. A total of 21 measurements were made on the twenty one zircon crystals (Table 6.1). The U content varies from 65 to 161 ppm and Th from 18 to 70 ppm. One zircon analysis produced a concordant data point with $^{206}Pb/^{238}U$ age of 707 $\pm$ 10 Ma, interpreted as that as xenocryst derived from older source material. Omitting three analyses with high common Pb and/or discordant leaves seventeen tightly grouped and concordant analyses that define a concordia age of 677 $\pm$ 8 Ma (95% conf.; MSWD = 0.91; Fig. 6.3a). We interpret this as the age of intrusion and crystallization of the diorite.

Sample B-mine (N24° 59′ 21.5″, E41° 35′ 51.6″) is a quartz-diorite collected from Bulghah mine area (Fig. 6.2). Zircon extracted from this sample is mostly euhedral, clear to yellow-brown, prismatic ($\sim$200 μm $\times$ 50 μm) and show well-developed oscillatory zoning consistent with a magmatic origin. One analysis was made on each of 10 zircons (Table 6.1) and these are presented on a concordia plot (Fig. 6.3b). Zircon U contents are low (58–163 ppm) and Th/U is low (0.3–0.4; Table 6.1). One analysis is concordant and has low Th content (16 ppm) and yields a $^{206}Pb/^{238}U$ age of 746 $\pm$ 14 Ma, higher than the 9 analyses, interpreted to represent an inherited grain from the older rocks in the area. The remaining nine analyses are concordant, defining a concordia age of 667 $\pm$ 6 Ma (2σ; MSWD = 2.3; Fig. 6.3 b). This age is identical to the age of the previous diorite sample (B139) and is interpreted as the crystallization age of the quartz-diorite.
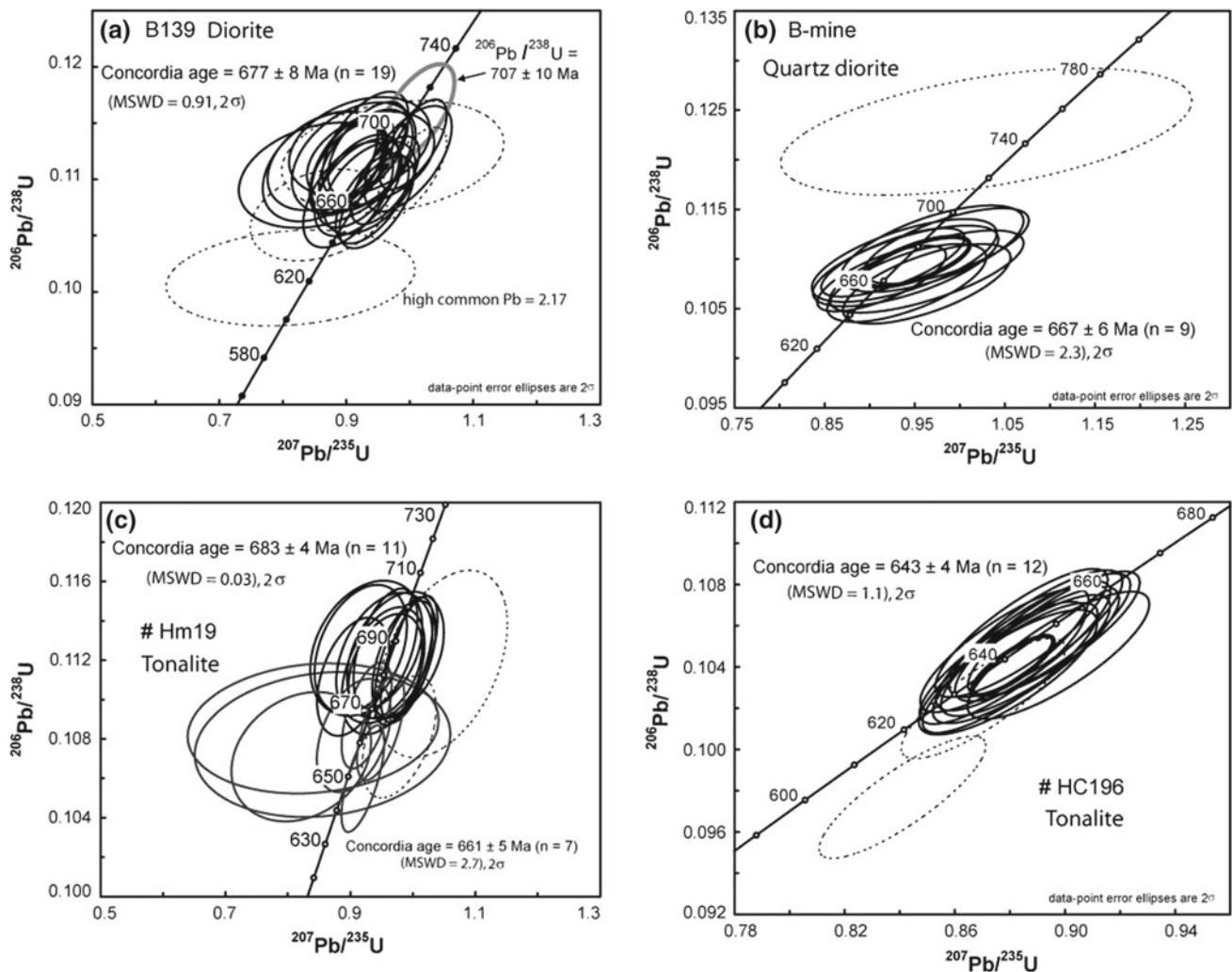
Fig. 6.3 U–Pb concordia diagrams of ion microprobe (SHRIMP) and laser-ablation inductively coupled plasma source mass spectrometry (LA-ICP-MS) data for zircons studied from the Bulghah and Humaymah areas. Dashed ellipses indicate zircon analyses that were excluded from age calculations. Errors for data ellipses are 2σ. Analytical data are given in Tables 6.1 and 6.2

Sample Hm19 (N24° 42′ 11.3″, E41° 42′ 57.8″) is medium to coarse-grained tonalite from Humaymah area (Fig. 6.2). Zircon recovered from this sample is subhedral to euhedral and yellow to pale brown. Zircon grains are idiomorphic, slender, and needle shaped, and exhibit well-preserved oscillatory growth zoning. These zircons contain moderate U contents (76–325 ppm) and have Th/U in the range expected for igneous zircons (0.2–0.5). Out of twenty-one zircon grains analyzed (Table 6.1), eleven analyses yield a concordia age of 683 ± 4 Ma (2σ, MSWD = 0.03), interpreted to represent inheritance from older rocks in the area. Three analyses are discordant and excluded from age calculation (Fig. 6.3c). Seven analyses were done on the rims of the same zircon grains produced a concordant data points and yield a concordia age of 661 ± 5 Ma (2σ, MSWD = 2.7; Fig. 6.3c), interpreted

to represent the crystallization age of the tonalite intrusion.

Sample HC196 (N24° 43′ 01.5″, E41° 43′ 2.5″) is coarse-grained tonalite from Humaymah (Fig. 6.2). Zircon recovered from this sample is subhedral to euhedral and yellow to pale brown. Zircon grains are idiomorph, slender, and needle shaped, and exhibit well-preserved oscillatory growth zoning. Out of fourteen zircon grains analyzed (Table 6.2), twelve analyses yielded a concordia age of 643 ± 4 Ma (2σ, MSWD = 1.1), interpreted to represent the age of the tonalite. Two analyses are discordant and excluded from age calculation (Fig. 6.3d). This age is indistinguishable from the age of a quartz diorite sample (629 ± 6 Ma; Harbi et al. 2018) in the Sukhaybarat area (70 km north of the study area) and the age of a monzogranite sample (631 ± 1 Ma) from Bulghah area (Bakhsh, unpublished data).

6.4.2 Whole-Rock Geochemistry

The results of chemical composition of 53 whole-rock samples from Bulghah and Humaymah areas are listed in Table 6.3. We compared our results with previous geochemical data of the I-type intrusive rocks (Figs. 6.5, 6.6, 6.7, 6.8, 6.9, 6.10, 6.11, 6.12 and 6.13) from Harbi et al. (2016, 2018) and Robinson et al. (2015). The intrusive samples from Bulghah show wide variations (in wt%) of SiO_2 (51.4–74.7), Al_2O_3 (12.39–19.95), CaO (1.05–9.95), Na_2O (3.10–5.85), MgO (0.30–6.50), Fe_2O_3t (1.06–7.41), and TiO_2 (0.18–1.02) (Table 6.3, Fig. 6.4). The K_2O content
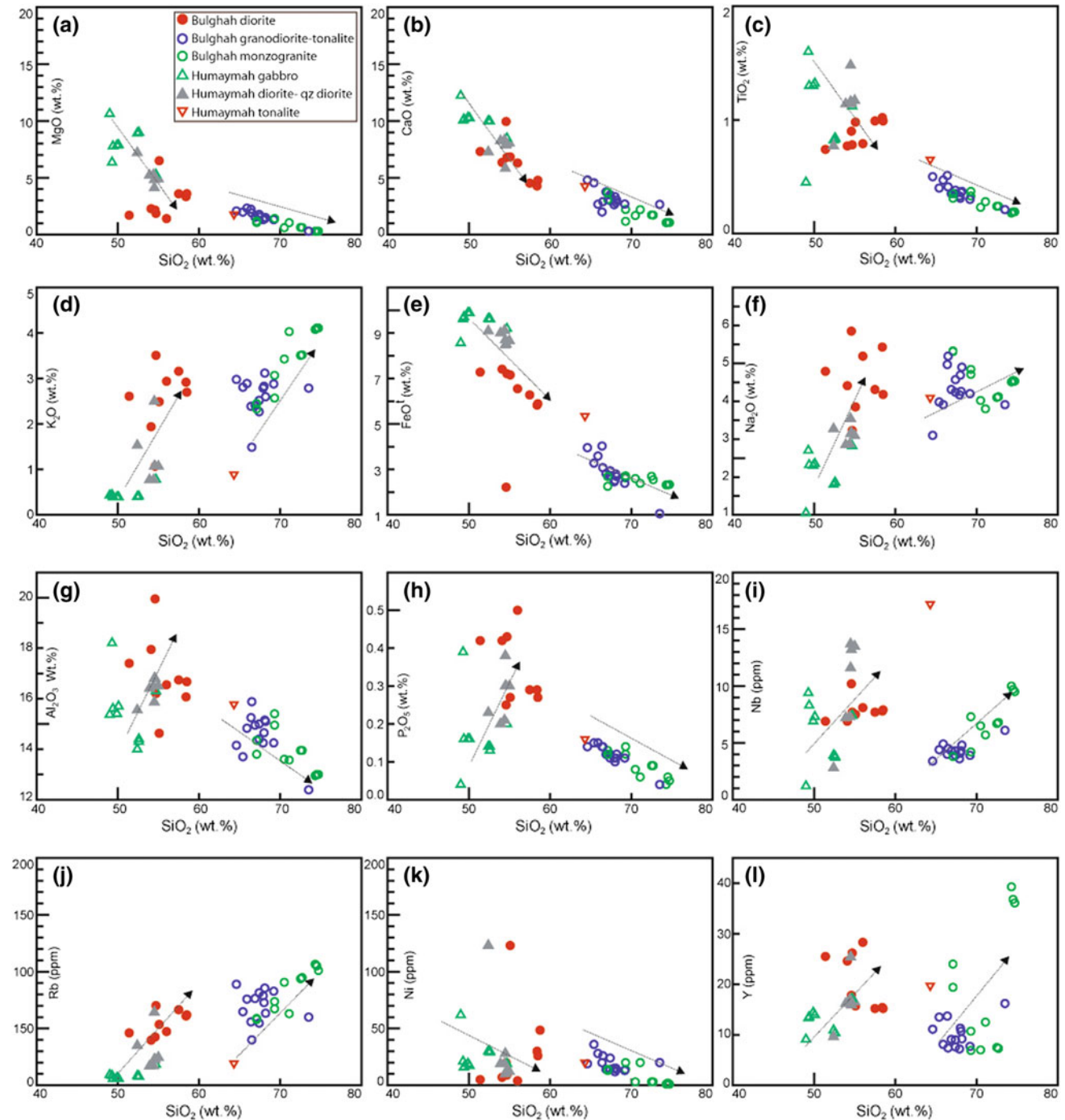
Fig. 6.4 Major and trace element variations diagrams (Harker diagrams) for the gabbro, diorite, tonalite, granodiorite and monzogranites define two different trends and showing compositional gap between the mafic intrusive rocks (gabbro and diorite) and granitoids (granodiorite-tonalite and monzogranite)
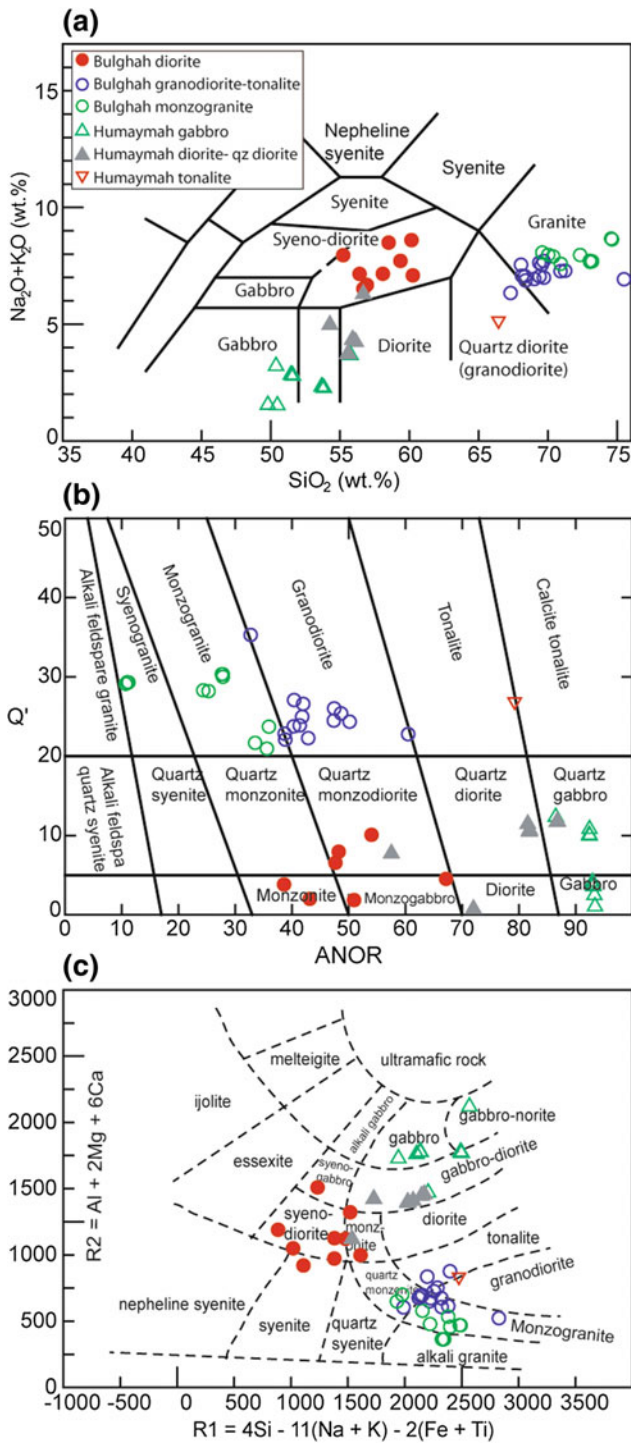
Fig. 6.5 Major and trace elements chemical classification diagrams. **a** Total alkalis (Na₂O + K₂O) versus SiO₂ (Cox et al. 1979), **b** The Q'–ANOR plutonic rocks classification diagram using their molecular normative compositions (after Streckeisen and Le Maitre 1979), **c** R1-R2 diagram (de la Roche et al. 1980). The field of Sukhaybarat I-type granitoids from Harbi et al. (2018) and the field of Jabal Ghadarah I-type granitoids from Harbi et al. (2016). Analytical data are given in Table 6.2
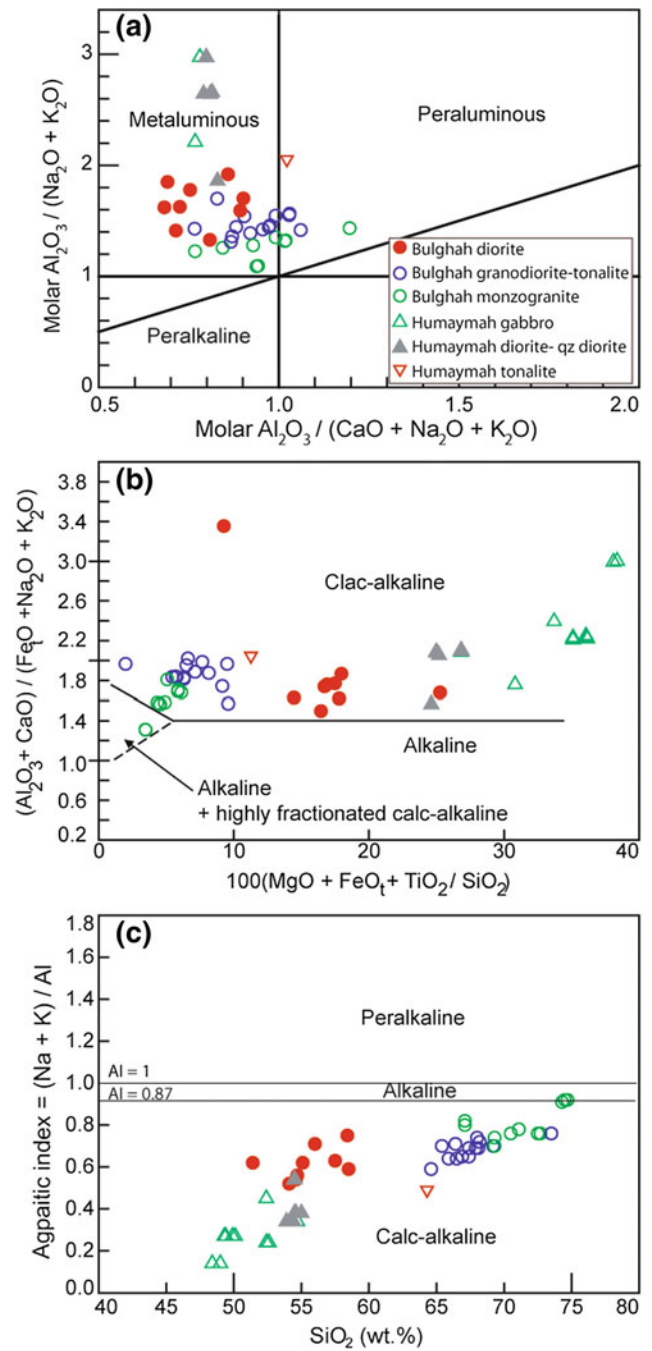
Fig. 6.6 a Shand's index (Maniar and Piccoli 1989) classification diagram, showing the intrusive studied samples exhibit metaluminous to slightly peraluminous geochemical features. **b** (Al₂O₃ + CaO/FeOₜ + Na₂O + K₂O) versus 100(MgO + FeOₜ + TiO₂ + SiO₂) discrimination diagram (Sylvester 1998) showing the predominantly calc-alkaline to highly fractionated calc-alkaline characteristics of the studied samples. **c** Agpaitic index (AI = Na + K/Al) versus SiO₂ diagram showing the calc-alkaline characters of the studied intrusive samples, the line with AI = 0.87 (Liégeois and Black 1987) separates alkaline and calc-alkaline granite series. The field of Sukhaybarat I-type granitoids from Harbi et al. (2018) and the field of Jabal Ghadarah I-type granitoids from Harbi et al. (2016)
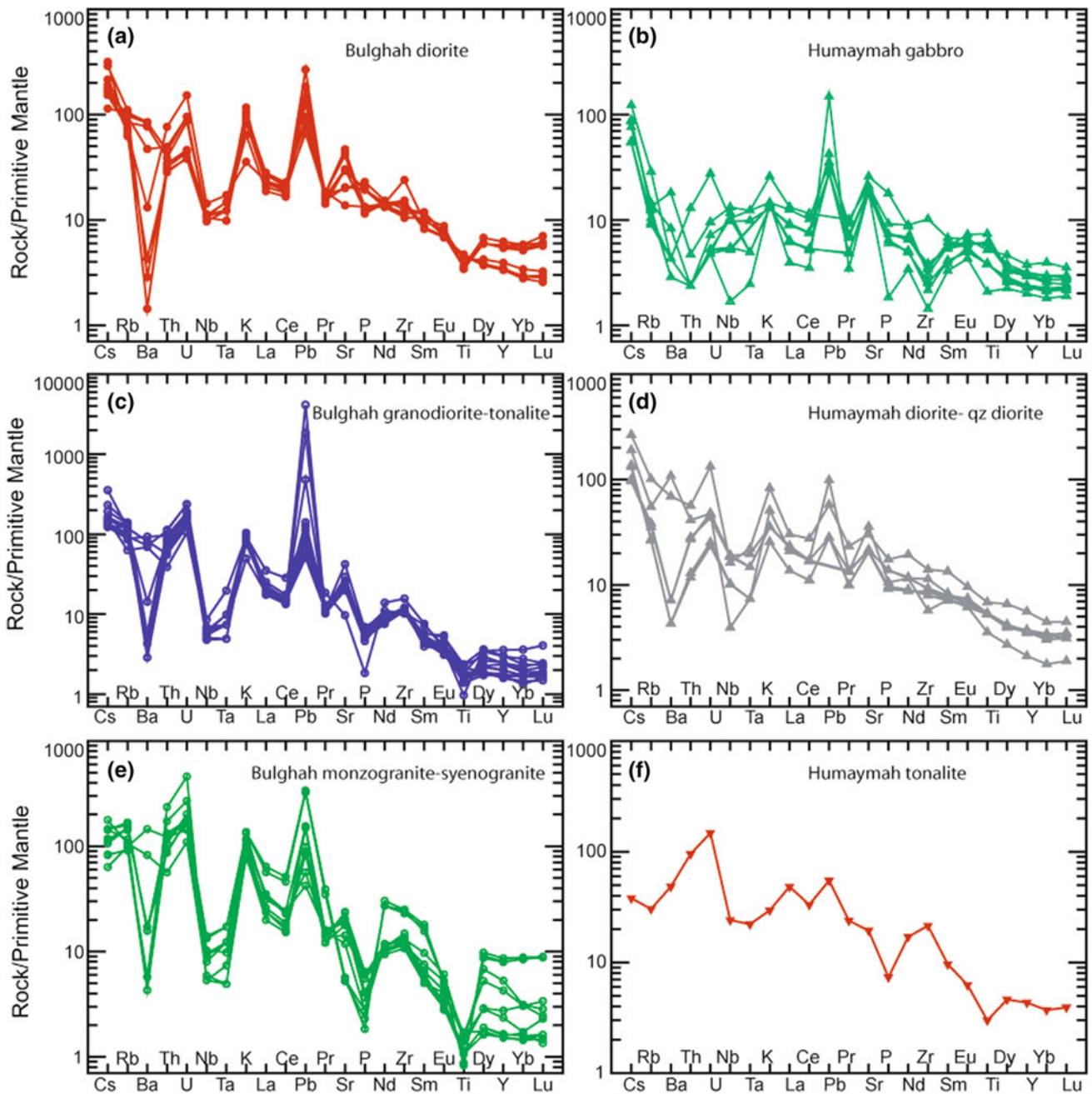
Fig. 6.7 Primitive mantle-normalized trace element diagrams for the studied Bulghah and Humaymah samples. Normalizing values from Sun and McDonough (1989)

indicates that the studied samples are high-K calc-alkaline (1.07–4.11 wt%; Fig. 6.4d). The intrusive rocks from Humaymah are more mafic than samples from Bulghah area. They exhibit variable variations (in wt%) of SiO_2 (48.4–64.3), Al_2O_3 (14.0–19.33), CaO (4.26–12.22), Na_2O (1.05–4.09), and high TiO_2 (0.45–1.60), MgO (1.78–10.64) and Fe_2O_3t (5.35–9.89) (Table 6.3, Fig. 6.4). The intrusive rocks have been classified using the total alkalis versus silica (Cox et al. 1979), Q′–ANOR diagram of Streckeisen and Le

Maitre (1979) and R1-R2 diagram of de la Roche et al. (1980). The intrusive samples of Bulghah plot in the monzogranite–synogranite, granodiorite-tonalite and syenodiorite fields (Fig. 6.5), whereas the Humaymah intrusive samples fall in the diorite, quartz diorite, gabbro and quartz gabbro fields, and one sample (Hm 19) plots in the tonalite field (Fig. 6.5).

According to Shand's index (Maniar and Piccoli 1989) classification diagram, the studied mafic intrusive samples

(gabbro and diorite-quartz diorite) from Bulghah and Humaymah are strongly metaluminous, whereas the granitoid rocks (granodiorite, tonalite and monzogranite) are strongly metaluminous to slightly peraluminous (Fig. 6.6a). On the major element discrimination diagram of Sylvester (1998), the studied intrusive rocks are calk-alkaline (Fig. 6.6b). They also fall in the calc-alkaline field (AI <

0.87; Fig. 6.6c) according to Liégeois and Black (1987). Three monzogranite samples (B46, B49 and B50) fall in the alkaline and highly fractionated calc alkaline field in both diagrams (Fig. 6.6b, c).

Primitive mantle normalized trace-element patterns for all intrusive samples from Bulghah and Humaymah are enriched in incompatible elements, showing negative anomalies
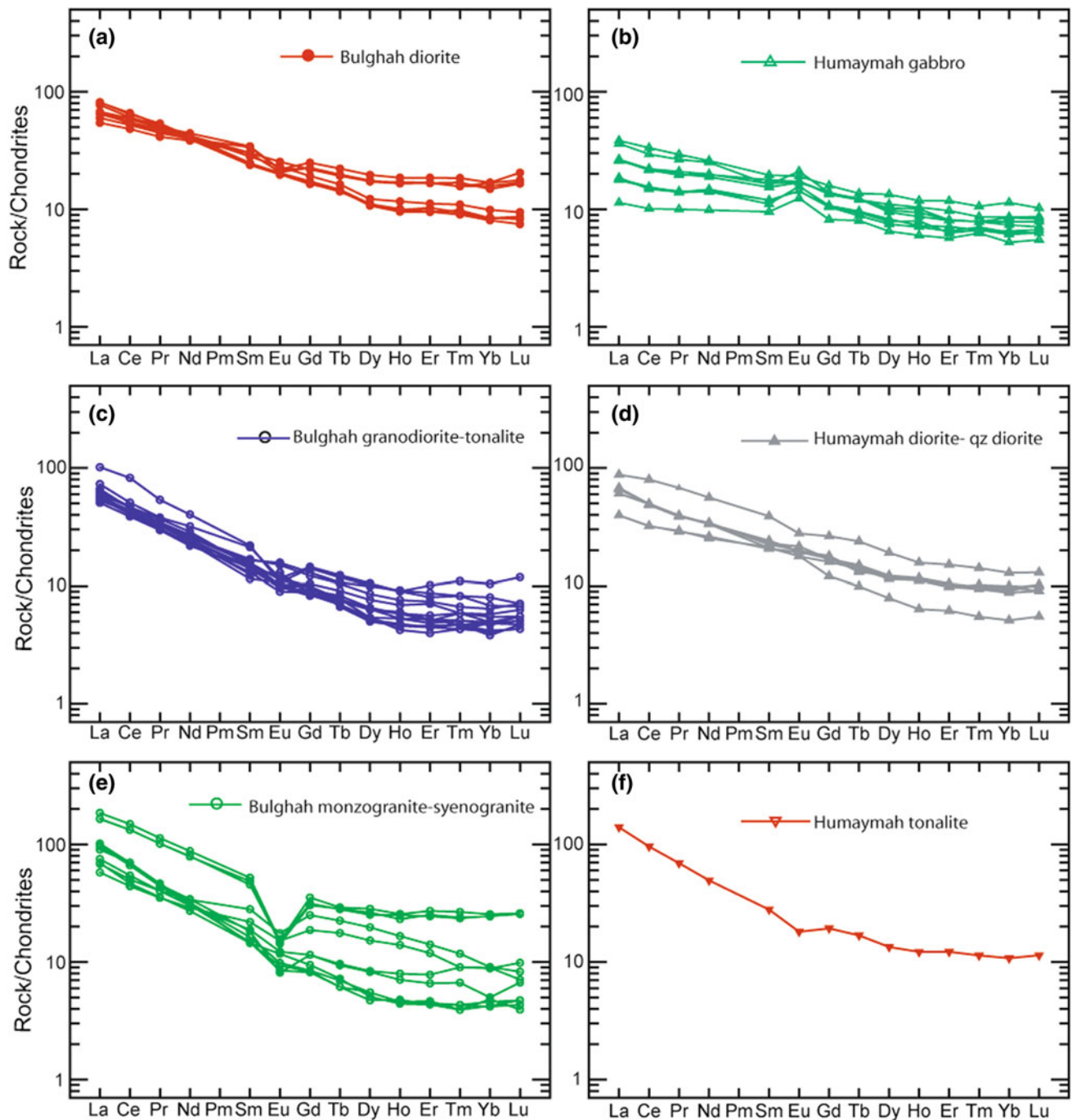
Fig. 6.8 Chondrite normalized REE patterns for the studied Bulghah and Humaymah samples. Normalizing values from Sun and McDonough (1989)

in Nb–Ta, Ti and P and a positive Pb anomaly (Fig. 6.7). The mafic and granitoid rocks in the studied areas have variable $Al_2O_3/(CaO + Na_2O + K_2O)$ molar ratios (A/CNK), mostly less than 1.1 (Fig. 6.6a), which is typical of I-type magmatism (Chappell 1999). The trace element

Fig. 6.9 a Th versus U, b Ta versus Nb, and c Hf versus Zr variation diagrams of the studied intrusive samples from the Bulghah and Humaymah areas, showing geochemical positive correlation between the different granitic types, suggesting that the behavior of these trace elements are largely controlled by magmatic processes. The field of Sukhaybarat I-type granitoids from Harbi et al. (2018)

patterns (Fig. 6.7) are typical of those developed in island arc settings (Elliott 2003; Ali et al. 2015).

The granodiorite-tonalite and monzogranite samples are both LREE and MREE enriched [(La/Yb)$_N$ = 6.12 − 21.70], with slightly fractionated HREE patterns [(Dy/Yb)$_N$ = 0.93 − 2.13] and minor negative to slightly positive Eu (Eu/Eu* = 0.35 − 1.25) and positive Sr anomalies (Figs. 6.7 and 6.8) which are indicative of feldspar fractionation. The diorite-quartz diorite samples are LREE and MREE enriched [(La/Yb)$_N$ = 3.38 − 11.24], with flat to slightly fractionated HREE patterns [(Dy/Yb)$_N$ = 1.00 − 1.63] and minor negative to slightly positive Eu (Eu/Eu* = 0.75 − 1.29) and positive Sr anomalies (Figs. 6.7 and 6.8). However, the Humaymah gabbro samples show almost flat REE patterns [(La/Yb)$_N$ = 2.06 − 4.67 and (Dy/Yb)$_N$ = 1.14 − 1.28], indicating that garnet did not control elemental partitioning during melting or fractionation, with positive Eu (Eu/Eu* = 1.08 − 1.43) and Sr anomalies (Figs. 6.7 and 6.8), and overall REE abundance is lower.

The variation of Th and U show strong positive correlations (Fig. 6.9a) which indicates magmatic behavior of Th and U during magmatic differentiation (Moghazi et al. 2011). Moreover, the variation of Ta versus Nb, and Hf versus Zr (Fig. 6.9b, c) show positive correlation, suggesting that the behavior and enrichment of Nb and Ta are largely controlled by magmatic process (Lehmann and Mahawat 1989; Charoy and Nornoha 1991).

6.5 Discussion

New U–Pb zircon ages and geochemical data that characterize the Bulghah and Humaymah areas, when combined with available geochemical data from previous studies (Harbi et al. 2016, 2018; Robinson et al. 2015), allow us to discuss their tectonic setting and their petrogenesis.

6.5.1 Tectonic Stetting

Granitic rocks are divided into I-, S- and A-types (Whalen et al. 1987; Chappell and White 1992, 2001). A-type granites contain high temperature hydrous phases such as pyroxene and fayalite, and late crystallization biotite and alkali amphibole (Wormald and Price 1988; King et al. 1997). However, petrographic investigation indicates that Bulghah and Humaymah granites show no pyroxene or fayalite, and contain hornblende which is inconsistent with alkali amphibole in typical A-type granites. Moreover, the slight enrichment in high field strength element (HFSE) and REE concentrations, in combination with the petrographic characteristics and the slight low Zr, Nb, Ce and Y

concentrations in most granitic samples, suggest that the studied samples are not A-type granites. The studied granitoids are not also S-type granites because they are metaluminous to slightly peraluminous, and have A/CNK < 1.1 and A/NK > 1 (Fig. 6.6a). It show also that P_2O_5 decreases with increasing SiO_2 (Fig. 6.4h). Additionally, the studied samples contain no Al-rich minerals such as cordierite, muscovite or garnet which are considered the common features of S-type granites (Chappell and White 1992; Huang et al. 2013).

Except for three samples, the granitoid rocks of Bulghah and Humaymah fall in the magnesian field on $FeO^t/FeO^t + MgO$ versus SiO_2 diagram (Frost et al. 2001) (Figure not shown). They are classified as I-type granites on the $10,000 \times Ga/Al$ versus Zr diagram (Whalen et al. 1987) (Fig. 6.10a). Rb, Ta, Nb and Y, among other trace elements, have been used to discriminate the different tectonic setting of granitoid rocks (Pearce et al. 1984). The studied granitoids fall in the volcanic-arc/syn-collisional fields (VAG + syn-COLG) in the Y + Nb versus Rb, Y versus Nb, and Yb versus Ta diagrams (Fig. 6.10b–c) of Pearce et al. (1984).

Mafic intrusive rocks (gabbro and diorite) have been classified using the Cr versus Y diagram (Fig. 6.10a; Pearce et al. 1984) and Cr versus Ce/Sr diagram (Fig. 6.10b; Pearce 1982), they plot in the island arc tholeiites (IAT) field. However, V versus Ti/1000 discrimination diagram ((Fig. 6.7c; Shervais 1982) classify the gabbro and diorite samples as mid-ocean ridge (MORB)/back-arc basin (BAB) mafic components. In summary, variation in multi-elements diagrams (Fig. 6.7) and REE discrimination diagram (Figs. 6.10 and 6.11) indicates that the studied rocks are related to calc-alkaline I-type magmatism formed in an island-arc setting.

6.5.2 Petrogenetic Evaluation

The main compositional trends of the studied intrusive rocks are shown on Harker variation diagrams (Fig. 6.4). The figure shows that many elements do not have straight-line variations (e.g., Al_2O_3, MgO, CaO, TiO_2, Na_2O, P_2O_5, Nb, Ni and Y) but exhibiting compositional gap between different intrusive types. This suggest two different

Fig. 6.10 Major and trace elements tectonic discrimination diagrams. **a** Rb versus Y + Nb, **b** Nb versus Y and **c** Ta versus Yb diagrams (after Pearce et al. 1984), showing the studied granitoids plot in the VAG field. **d** Zr versus 10,000 Ga/Al diagram (Whalen et al. 1987), showing the studied intrusive fall in the I-type granite field. However, few monzogranite samples fall in the A-type field, perhaps due to the mobility of Al (major element). Note diorite intrusive samples are also plotted to highlight the compositional range within these suites, but are classified in Fig. 6.11. VAG = volcanic arc granite, syn-COLG = syn-collision granite, ORG = ocean ridge granite, WPG = within plate granite and post-COLG = post-collisional granite. The field of Sukhaybarat I-type granitoids from Harbi et al. (2018) and the field of Jabal Ghadarah I-type granitoids from Harbi et al. (2016)
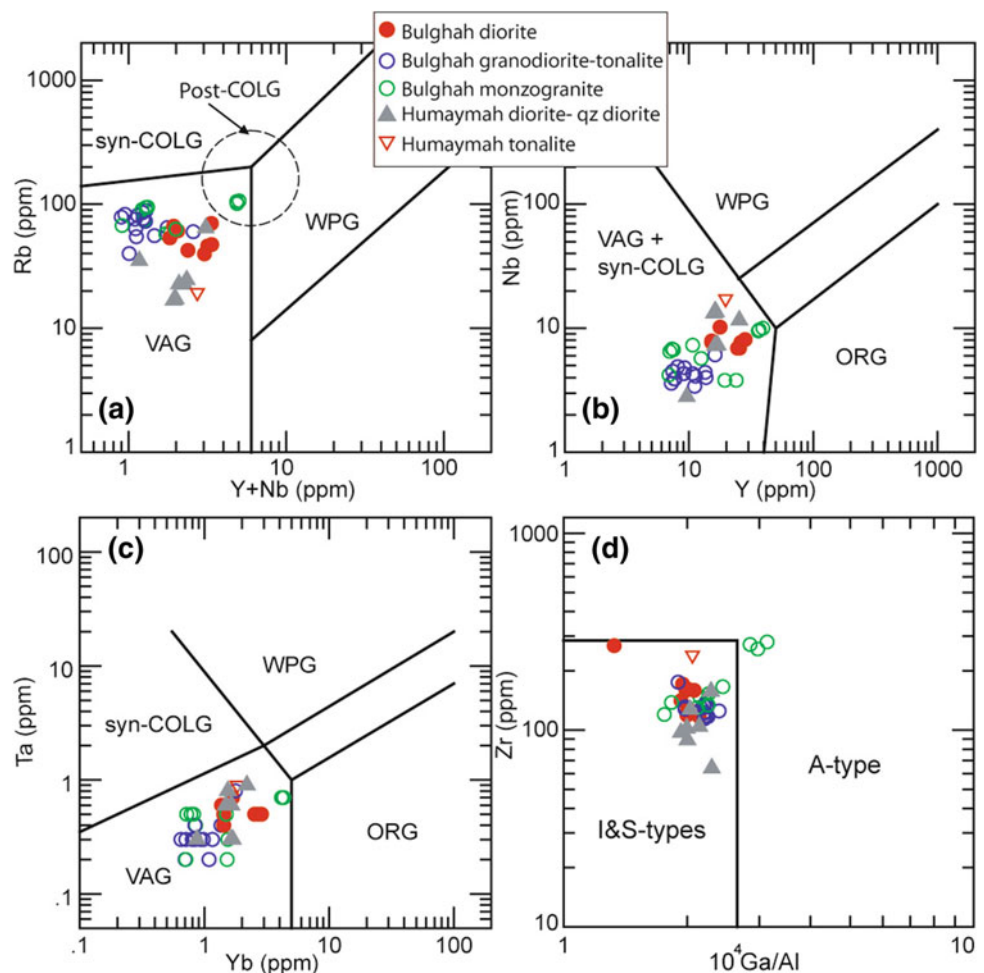
Fig. 6.11 Mafic intrusive classification schemes applied to gabbroic and dioritic samples from Bulghah and Humaymah areas. **a** Cr versus Y and **b** Cr versus Ce/Sr (after Pearce et al. 1984), showing the studied samples fall in the IAT field. **c** V versus Ti/1000 (after Shervais 1982), showing the studied samples plot in the IAT, MORB and BAB fields. The field of Makkah Suite mafic intrusive rocks (Jeddah terrane) from Robinson et al. (2015). Results are discussed in text. MORB = mid-ocean ridge basalt, BAB = back-arc basalt, and IAT = island-arc tholeiitic
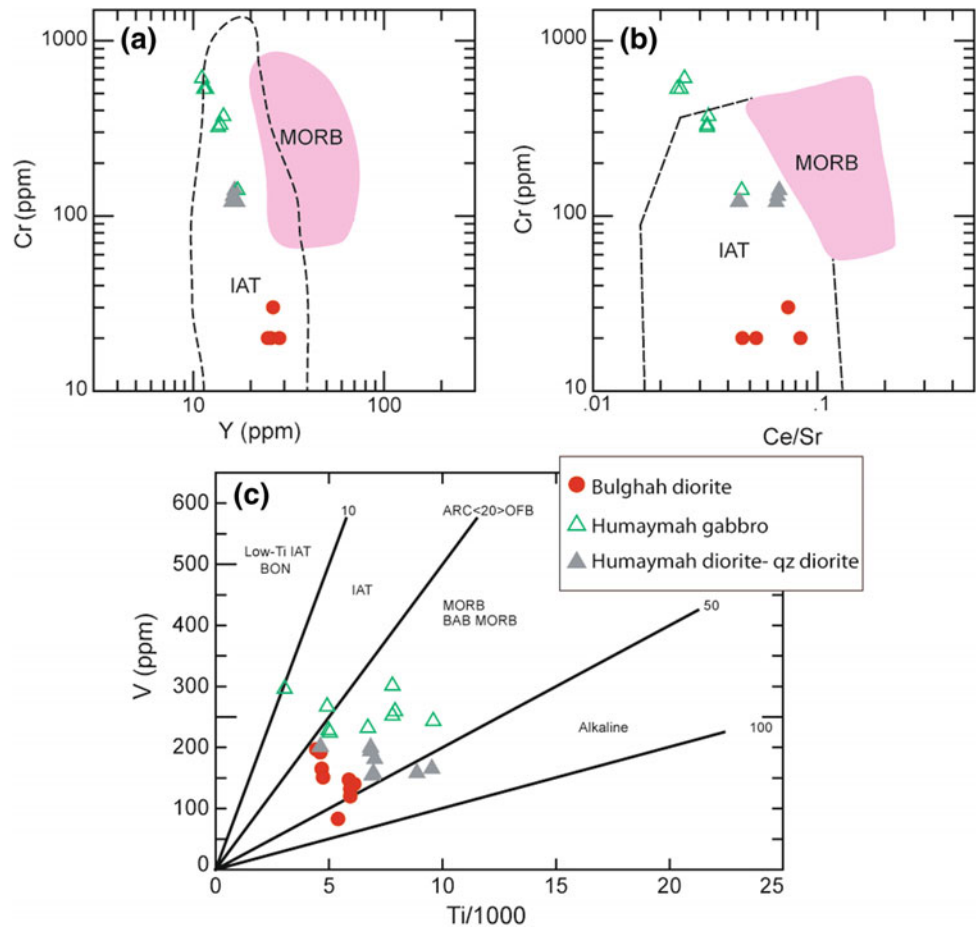
compositional trends in Bulghah and Humaymah intrusive rocks; one for gabbro and diorite and the other for granodiorite-tonalite and monzogranite. Overall, the mafic intrusive rocks are characterized by slightly LREE enriched patterns and relatively flat HREE patterns $[(Dy/Yb)_N = 1.00 − 1.33$, except for three diorite samples show higher values $[(Dy/Yb)_N = 1.45 − 1.63)$ (Fig. 6.8a, d, e). Most samples show Cs, Sr, Rb and K enrichments and Nb, Ta and Ti depletions. The gabbroic samples have La/Nb ratios range from 0.9 to 2.3 and slightly LREE enriched $[(La/Yb)_N = 2.06 − 4.67]$ (Fig. 6.8), although all mafic samples (gabbro and diorite) are outside this range $[(La/Yb)_N = 2.06 − 11.24]$. All mafic intrusive samples show negative Ce and positive or slightly negative Eu anomalies (Eu/Eu* = 0.75 − 1.43) (Figs. 6.7 and 6.8). These geochemical features are comparable to those of the arc-metavolcanic calc-alkaline rocks of the Arabian Shield (Ali et al. 2010), which were produced by partial melting of plagioclase- or spinel-peridotite in the upper most mantle <80 km deep in an intra-oceanic island arc, as indicated from the flat HREE patterns (Rudnick et al. 2004) and other trace element characteristics (Ali et al. 2010). This suggests that the mafic intrusive rocks of Bulghah and Humaymah

represent the plutonic equivalents of the Arabian Shield arc metavolcanic calc-alkaline rocks.

I-type granitoids can be formed through number of magmatic processes (e.g., Miller 1985; Jiang et al. 2007; Hassanen et al. 1996; Best and Christiansen 2001; Roberts and Clements 1993; Skjerlie and Johnston 1992; Frost and Frost 1997; Clemens et al. 2011; Chappell et al. 2012; Huang et al. 2013; Zhang et al. 2015), including Derivation from magmas generated by partial melting of mafic and intermediate igneous rocks has been proposed for some I-type granitoids (see Best and Christiansen 2001). Others have suggested that the I-type granitoids derived from partial melting of ancient lower crust (e.g., Jiang et al. 2007) or hydrous, calc-alkaline to high-K calk-alkaline old metamorphic rocks (Roberts and Clements 1993). Several studies proposed fractional crystallization of mafic/intermediate magmas as an important process to generate felsic magmas (e.g., Miller and Mittlefehlt 1984; Miller 1985; Secchi et al. 1991; Teixeira et al. 2012). Partial melting of eclogite or garnet amphibolite at mantle depth (Hassanen et al. 1996) and dehydration melting of amphibole-bearing tonalite (Creaser et al. 1991; Skjerlie and Johnston 1992; Frost and Frost 1997) are other potential sources to generate I-type

granites. Differentiation (i.e. partial melting and/or fractional crystallization) of crust and then the magma may have been modified to a degree by fractional crystallization (Miller 1985; Turpin et al. 1990; Barbarin 1996; Champion and Chappell 1992; Chappell et al. 2012; Zhang et al. 2015) could be another source for the I-type granites.

The I-type granitoids (granodiorite-tonalite to monzo-granite) of the current study cannot account as a product of mafic magma fractionation since Harker diagrams exhibiting compositional gap between different intrusive types (Fig. 6.4). This exclude the possibility that the granitoids were produced from magmas generated by partial melting of mafic igneous rocks. This is further supported by the U–Pb geochronology data, the dioritic rocks yielded U–Pb ages of 677 ± 8 Ma and 667 ± 6 Ma (Fig. 6.3), whereas the U–Pb zircon age of the monzogranite intrusion is 631 ± 1 Ma

(Bakhsh, unpublished data). A large span in U–Pb ages from 677 (mafic rocks) to 631 (intermediate and felsic rocks) implies that the granodiorite and monzogranite originated from a different magma source than that of the mafic magma (gabbro and diorite).

The compositional variations from granodiorite-tonalite to monzogranite of Bulghah and Humaymah perhaps caused by varying degree of partial melting suggest various degree of fractional crystallization. Varying degree of partial melting of a source could effectively produce melts that have diverse concentration of both major and trace elements (Huang et al. 2013). The most felsic rocks (monzogranite) representative of the lowest degree of partial melting of a source should have the highest La/Yb but lowest Dy/Yb (Huang et al. 2013). However, monzogranite and granodiorite samples show scattered ratios (Fig. 6.12a), inconsistent
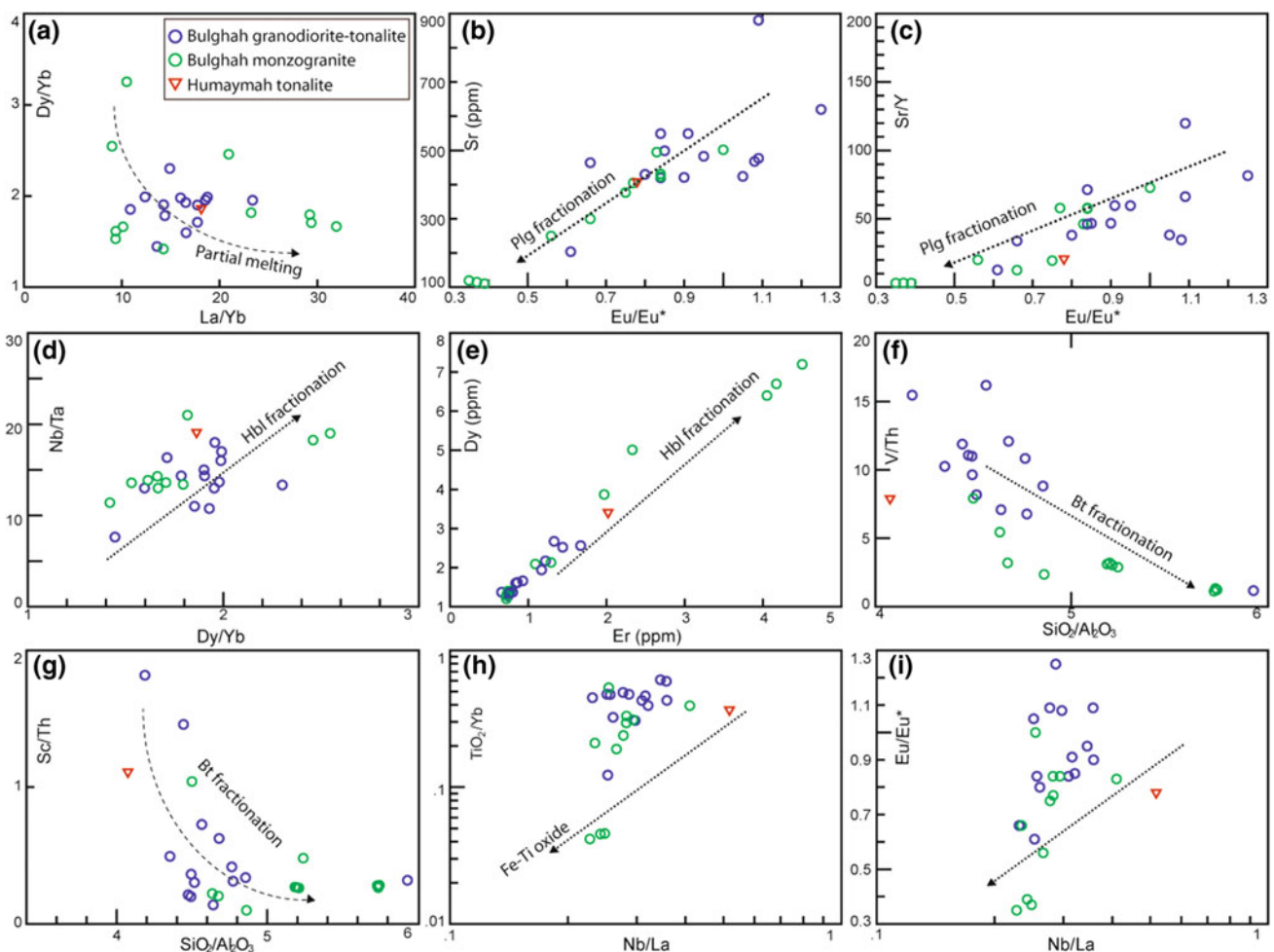
Fig. 6.12 **a** Dy/Yb versus La/Yb compositional variation diagram, indicating that the studied granitoid samples inconsistent with the partial melting trend. **b** Sr versus Eu/Eu* and **c** Sr/Y versus Eu/Eu* variation diagrams, showing that fractionation of plagioclase played an important role in the differentiation of the studied I-type granitoids. **d** Nb/Ta versus Dy/Yb and **e** Dy versus Er variation diagrams, showing that fractionation of hornblende played an important role in the differentiation of the studied I-type granitoids. **f** V/Th versus SiO_2/Al_2O_3 and **g** Sc/Th versus SiO_2/Al_2O_3 variation diagrams, suggesting biotite fractionation between granodiorite and monzogranite samples. **h** TiO_2/Yb versus Nb/La and **i** Eu/Eu* versus Nb/La diagrams for the granitoid samples, showing no correlation indicate a minor role of Fe–Ti oxides fractionation in the genesis of the granodiorites and monzogranites

with the partial melting trend. Thus, it is unlikely that varying degree of partial melting is responsible for the diverse elemental concentrations in Bulghah grantoid rocks. Partial melting model of garnet amphibolite at mantle depth (Hassanen et al. 1996) generates a peraluminous melt (Beaard and Lofgen 1991). However, the studied granitoid samples are metaluminous to weakly peraluminous, indicating water undersaturated partial melting (Huang et al. 2013). Garnet with plagioclase and orthopyroxene would be major residual phases at high pressure (Wolf and Wyllie 1994). If garnet is a residual phase in the source, the HREE patterns will show strong depletion, but the studied granitoid samples show flat to slightly depleted HREE (Fig. 6.8b, c, f). Therefore, the possibility of a high pressure magma source can be excluded as a source for the studied granitoid samples. Contrasting REE patterns between the granodiorite-tonalite and monzogranite samples may have resulted from various degree of fractional crystallization. K-feldspar separation is responsible for the depletion of Ba (Wu et al. 2002; Fig. 6.7c, e), whereas Plagioclase fractionation depleted Eu and Sr in the melts (Figs. 6.7 and 6.8). As shown by Sr, Sr/Y versus Eu/Eu* (Fig. 6.12b and c), the correlations observed in Bulghah granite samples are indicative of plagioclase fractionation. Fractionation of amphibole will lower the Nb/Ta and Dy/Yb ratios in the remaining melt because of its D(Nb)/D(Ta) > 1 (Tiepolo et al. 2001) and D(Dy)/D(Yb) > 1 (Sisson 1994). A positive correlation between Nb/Ta and Dy/Yb in the Bulghah I-type granitoids strongly suggests amphibole fractionation (Fig. 6.12d). This is further confirmed by the positive correlation between Er and Dy corresponds to the fractionation of hornblende from the parental magma (Drummond et al. 1996; Fig. 6.12e). Biotite have a low value for Th, but high partition coefficients for Sc and V (Bea et al. 1994), therefore biotite fractionation will increase SiO_2/Al_2O_3 but decrease Sc/Th and V/Th ratios in residual melts (Huang et al. 2013). Thus, negative correlations between V/Th and Sc/Th and SiO_2/Al_2O_3 (Fig. 6.12f, g), perhaps indicate biotite fractionation between granodiorite and monzogranite samples of Bulghah. Ti-bearing minerals, such as titanite and ilmenite, might be other fractionated phases as suggested by increasing TiO_2 with decreasing SiO_2 (Huang et al. 2008; Table 6.3, Fig. 6.4c). The fractional crystallization of titanium-rich minerals commonly generates negative Nb–Ta and Ti anomalies in basalts (Xiong et al. 2005; Huang et al. 2008). However, this cannot be the reason for low Nb–Ta (Fig. 6.8b) in the studied granitoids because there are lack of correlations between TiO_2/Yb, Eu/Eu* and Nb/La (Fig. 6.12h, i), indicating a minor role of Fe–Ti oxide fractionation in the genesis of the studied granitoids. Therefore, various degrees of plagioclase, hornblende and biotite fractional crystallization would be important mechanism for variations in chemical composition of the studied granitoids (Fig. 6.12a–

i). The wide range of Mg# (14.5–40.2), Ni (<1–36 ppm) and V (11–89 ppm) contents of the studied granitoids (Table 6.3), perhaps suggest that two or more different
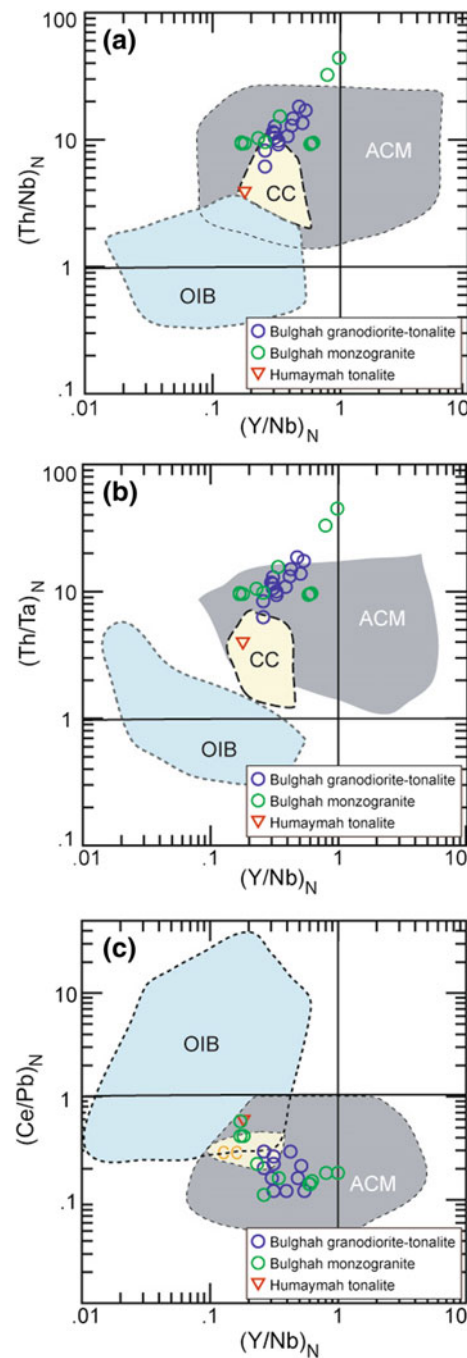
Fig. 6.13 Relationships of $(Th/Nb)_N$, $(Th/Ta)_N$, and $(Ce/Pb)_N$ versus $(Y/Nb)_N$ for the studied granitoid samples from the Bulghah and Humaymah areas with compositional fields of active continental margin (ACM), ocean island basalt (OIB) and continental crust (CC) from Moreno et al. (2014). The field of Sukhaybarat I-type granitoids from Harbi et al. (2018) and the field of Jabal Ghadarah I-type granitoids from Harbi et al. (2016). Normalization values are from McDonough and Sun (1995)

magma sources are likely for the granodiorites and monzo-granites (Kelemen 1995; Taylor and Mclennan 1985; Wang et al. 2014). This is supported by the relationships between Y/Nb with Th/Nb, Th/Ta and Ce/Pb (Fig. 6.13) which are sensitive to mantle and continental crust magma sources (Hofmann et al. 1986; Miller et al. 1994; Montero et al. 2009; Rudnick and Gao 2003; Rudnick et al. 2004; Moreno et al. 2014). The relationships of the Y/Nb with Th/Nb and Th/Ta (Fig. 6.13a, b) provide an efficient discrimination between oceanic island (OIB) and convergent margin (ACM) rock types. This is because that any change in incompatible trace-element ratios resulting from magmatic differentiation (e.g., crystal fractionation or partial melting) should be small in comparison to that which may result from two magma sources. The studied samples lie within the field of convergent margin magmatism and inside, or close to, the continental crust field (Fig. 6.13a and b). The $(Y/Nb)_N$ versus $(Ce/Pb)_N$ diagram also show that the granodiorite and the monzogranite samples have the features of a convergent margin and continental crust component (Fig. 6.13c). Therefore, these relationships (Fig. 6.13) suggest the significant involvement of a continental crust component in the granodiorites and monzogranites.

These rocks also show crustal-like trace-element patterns with negative Nb, Ta and Ti, and positive Pb anomalies (Fig. 6.7c, e, f). This is supported by Nb/Ta ratios ranging from (7.6 to 21.0, average of 14.5) that are close to the composition of magmas derived from crust and mantle (17.5; Green 1995). However, mixing model between mafic and felsic magmas needs to be confirmed by whole-rock Sr-Nd isotopes.

6.6 Conclusions

The following are the conclusions from our study:

1. Zircon U–Pb dating indicates that the mafic intrusive rocks from Bulghah and Humaymah, Saudi Arabia were formed at ~ 670 Ma, whereas the granitoid I-type intrusions were formed between 661 ± 5 and 643 ± 4 Ma, confirming the importance of the 700–640 Ma crustal forming event in Saudi Arabia.
2. Our analyses of the intrusive samples revealed no evidence of pre-Neoproterozoic zircons, further indicating that ANS crust in this region is mostly juvenile.
3. The studied intrusive rocks range in composition from gabbro-diorite to monzogranite. The gabbro-diorites and granodiorite-tonalite rocks are calk-alkaline, metaluminous to slightly peraluminous, whereas the monzogranite samples are classified as calc-alkaline to highly fractionated calc-alkaline.

4. The granodiorite-tonalite and monzogranite samples are I-type granites and classified as magnesian formed in a volcanic arc setting.
5. The mafic intrusive rocks (gabbro and diorite) formed in island arc setting, perhaps represent the plutonic equivalents of the Arabian Shield arc metavolcanic calc-alkaline rocks which were produced by partial melting of plagioclase- or spinel-peridotite in the upper most mantle <80 km deep in an intra-oceanic island arc.
6. Y/Nb with Th/Ta, Th/Nb Nb and Ce/Pb relationships indicated that the granodiorites-tonalies and monzogranites generated by a combination of mafic parental magma contaminated with crustal materials and controlled by fractional crystallization.

References

Agar RA (1985) Stratigraphy and paleogeography of the Siham group: direct evidence for a late Proterozoic continental microplate and active continental margin in the Saudi Arabian shield. J Geol Soc London 142:1205–1220

Agar RA (1986) The Bani Ghayy group; sedimentation and volcanism in "pullapart" grabens of the Najd strike-slip orogen, Saudi Arabian Shield. Precambrian Res 31:259–274

Agar RA (1988) Geologic map of the Zalm quadrangle, sheet 22 F, Kingdom of Saudi Arabia: Saudi Arabian Deputy Ministry for Mineral Resources Geologic Map Number GM 89, scale 1:250,000, 41 p

Agar RA, Stacey JS, Whitehouse MJ (1992) Evolution of the southern Afif terrane—a geochronologic study. Saudi Arabian Deputy Ministry for Mineral Resource, Open File Report DGMR-OF-10-15, 41 p

Ali KA, Andresen A, Stern RJ, Manton WI, Omar SA, Maurice AE (2012) U–Pb zircon and Sr-Nd–Hf isotopic evidence for a juvenile origin of the c 634 Ma El-Shalul Granite, Central Eastern Desert, Egypt. Geol Mag 149:783–797

Ali KA, Kröner A, Hegner E, Wong J, Li S-Q, Gahlan HA, Abu El Ela AA (2015) U–Pb zircon geochronology and Hf–Nd isotopic systematics of Wadi Beitan granitoid gneisses, South Eastern Desert, Egypt. Gondwana Res 27:811–824

Ali KA, Stern RJ, Manton WI, Kimura J-I, Khamees HA (2009) Geochemistry, Nd isotopes and U–Pb SHRIMP dating of Neoproterozoic volcanic rocks from the Central Eastern Desert of Egypt: New Insights into the ~ 750 Ma Crust-Forming Event. Precambrian Res 171:1–22

Ali KA, Stern RJ, Manton WI, Kimura J-I, Whitehouse MJ, Mukherjee SK, Johnson PR, Griffin WR (2010) Geochemical, U–Pb zircon, and Nd isotope investigations of the Neoproterozoic Ghawjah Metavolcanic rocks, Northwestern Saudi Arabia. Lithos 120: 379–393

Barbarin B (1996) Genesis of the two main types of peraluminous granitoids. Geology 24:295–298

Bea F, Pereira MG, Stroh A (1994) Mineral/leucosome trace-element partitioning in a peraluminous migmatite (a laser ablation-ICP-MS study). Chem Geol 117:291–312

Beard JS, Lofgren GE (1991) Dehydration melting and water-saturated melting of basaltic and andesitic greenstones and amphibolites at 1, 3, and 6.9 kbar. J Petrol 32:365–401

Be'eri-Shlevin Y, Katzir Y, Whitehouse M (2009) Post-collisional tectono-magmatic evolution in the northern Arabian-Nubian Shield (ANS): time constraints from ionprobe U–Pb dating of zircon. J Geol Soc London 166:71–85

Best MG, Christiansen EH (2001) Igneous Petrology. Blackwell Science Inc. 458 pp

Bonin B, Giret A (1990) Plutonic alkaline series: Daly gap and intermediate compositions for liquids filling up crustal magma chambers. Schweiz Mineral Petrogr Mitt 70:175–187

Brown FB, Schmidt DL, Huffman AC (1989) Geology of the Arabian Peninsula: shield area of Western Saudi Arabia. US Geological Survey Professional Paper 560-A, 188 p

Champion DC, Chappell BW (1992) Petrogenesis of felsic I-type granites: an example from northern Queensland. Trans R Soc Edinb Earth Sci 83:115–126

Chappel BW (1999) Aluminum saturation in I- and S-type granites and the characterization of fractionated haplogranites. Lithos 46:535–551

Chappell BW, White AJR (1992) I- and S-type granites in the Lachlan Fold Belt. Trans R Soc Edinb Earth Sci 83:1–26

Chappell BW, White AJR (2001) Two contrasting granite types: 25 years later. Aust J Earth Sci 48:489–499

Chappell BW, Bryant CJ, Wyborn D (2012) Peraluminous I-type granites. Lithos 153:142–153

Charoy B, Nornoha F (1991) The Argemella granite-porphyry (central Portugal): the subvolcanic expression of a high fluorine, rare-element pegmatite magma. In: Pagel M, Leroy JL (eds) Source, transport and deposition of metals. A.A. Balkema, Rotterdam, pp 741–744

Clemens JD, Stevens G, Farina F (2011) The enigmatic sources of I-type granites: the peritectic connexion. Lithos 126:174–181

Collins WJ, Beams SD, White AJR, Chappell BW (1992) Nature and origin of A-type granites with particular reference to southeastern Australia. Contrib Miner Petrol 80:189–200

Compston W, Williams IS, Meyer C (1984) U–Pb geochronology of zircons from lunar breccia 73217 using a sensitive high-resolution ion microprobe. J Geophys Res 89:B525–B534

Cox KG, Bell JD, Pankhurst RJ (1979) The interpretation of data for plutonic rocks, The interpretation of igneous rocks. Springer, Netherlands, pp 308–331

Creaser RA, Price RC, Wormald RJ (1991) A-type granites revisited: assessment of a residual source model. Geology 19:163–166

Delfour J (1977) Geological map of the Nuqrah quadrangle, 25E, Kingdom of Saudi Arabia. Saudi Arabian Dir. Gen. Miner. Resour. Geological Map GM 28, scale 1:250,000, 32 p

Delfour J (1981) Geological map of the Al Hissu quadrangle sheet 24 E, Kingdom of Saudi Arabia. Saudi Arabian Dir. Gen. Miner. Resour. Geological Map GM 58, scale 1:250,000, 47 p

de la Roche H, Leterrier J, Grandclaude P, Marchal M (1980) A classification of volcanic and plutonic rocks using R1R2 diagram and major-element analyses—its relationships with current nomenclature. Chem Geol 29:183–210

Dilek Y, Ahmed Z (2003) Proterozoic ophiolites of the Arabian Shield and their significance in Precambrian tectonics. Ophiolites Earth Hist Geol Soc Lond, Special Publications 218:685–701

Drummond MS, Defant MJ, Kepezhinskas PK (1996) Petrogenesis of slab derived trondhjemite-tonalite-dacite/adakite magmas. Trans R Soc Edinb Earth Sci 87:205–215

Eby GN (1990) The A-type granitoids: a review of their occurrence and chemical characteristics and speculations on their petrogenesis. Lithos 26:115–134

Eby GN (1992) Chemical subdivision of the A-type granitoids; petrogenetic and tectonic implications. Geology 20:641–644

Elliott T (2003) Tracers of the slab. In: Eiler J (ed) Inside the subduction Factory. Geophysical Monograph Series, vol 138. American Geophysical Union, Washington, pp 23–45

Eyal M, Litvinovsky B, Jahn B, Zanvilevich A, Katzir Y (2010) Origin and evolution of post-collisional magmatism: coeval Neoproterozoic calc-alkaline and alkaline suites of the Sinai Peninsula. Chem Geol 269:153–179

Frost CD, Frost BR (1997) Reduced rapakivi-type granites: the tholeiite connection. Geology 25:647–650

Frost BR, Barnes CG, Collins WJ, Arculus RJ, Ellis DJ, Frost CD (2001) A Geochemical classification for granitic rocks. J Petrol 42:2033–2048

Genna A, Nehlig P, Le Goff E, Gguerrot C, Shanti M (2002) Proterozoic tectonism of the Arabian Shield. Precambrian Res 117:21–40

Green TH (1995) Significance of Nb/Ta as an indicator of geochemical processes in the crust–mantle system. Chem Geol 120:347–359

Greiling RO, Abdeen MM, Dardir AA, El Akhal H, El Ramly MF, Kamal El Din GM, Osman AF, Rashwan AA, Rice AHN, Sadek MF (1994) A structural synthesis of the Proterozoic Arabian–Nubian Shield in Egypt. Geol Rundschau 83:484–501

Harbi HM, Ali KA, Eldougdoug AA, Al Jahdali NS (2016) $^{40}Ar/^{39}Ar$ and U–Pb zircon dating constraints along Bir Tawilah shear zone, central Saudi Arabia: implication for age of gold mineralization. Chem Erde 76:309–324

Harbi HM, Ali KA, McNaughton NJ, Andresen A (2018) U–Pb zircon and $^{40}Ar/^{39}Ar$ geochronology of sericite from hydrothermal alteration zones: new constraints for the timing of Ediacaran gold mineralisation in the Sukhaybarat area, western Afif terrane, Saudi Arabia. Miner Deposita 53:459–476

Hassanen M, El-Nisr S, Mohamed FH (1996) Geochemistry and petrogenesis of Pan-African granitoids at Gabal Igla Ahmar, Easter Desert, Egypt. J Afr Earth Sci 22:29–42

Hofmann AW, Jochum KP, Seufert M, White WM (1986) Nb and Pb in oceanic basalts: new constraints on mantle evolution. Earth Planet Sci Lett 79:33–45

Huang HQ, Li XH, Li WX, Li ZX (2011) Formation of high δ18O fayalite-bearing A-type granite by high-temperature melting of granulitic metasedimentary rocks, Southern China. Geology 39:903–906

Huang X-L, Xu Y-G, Li X-H, Li W-X, Lan J-B, Zhang H-H, Liu Y-S, Wang Y-B, Li H-Y, Luo Z-Y, Yang Q-J (2008) Petrogenesis and tectonic implications of Neoproterozoic, highly fractionated A-type granites from Mianning, South China. Precambrian Res 165: 190–204

Huang X-L, Yu Y, Li J, Tong L-X, Chen LL (2013) Geochronology and petrogenesis of the early Paleozoic I-type granite in the Taishan area, South China: middle-lower crustal melting during orogenic collapse. Lithos 117:268–284

Jackson SE, Pearson NJ, Griffin WL, Belousova EA (2004) The application of laser ablation-inductively coupled plasma-mass spectrometry to in-situ U–Pb zircon geochronology. Chem Geol 211:47–69

Jarrar G, Stern RJ, Saffarini G, Al-Zubi H (2003) Late- and post-orogenic Neoproterozoic intrusions of Jordan: implications for crustal growth in the northernmost segment of the East African Orogen. Precambrian Res 123:295–319

Jiang N, Liu Y, Zhou W, Yang J, Zhang S (2007) Derivation of Mesozoic adakitic magmas from ancient lower crust in the North China Craton. Geochim Cosmochim Acta 71:2591–2608

Johnson PR (1998) Tectonic map of Saudi Arabia and adjacent areas. Saudi Arabian Deputy Ministry for Mineral Resource, Technical Report USGS-TR-98-3, scale 1:40,000,000

Johnson PR (2003) Post-amalgamation basins of the NE Arabian shield and implications for Neoproterozoic III tectonism in the northern East African orogen. Precambr Res 123:321–338

Johnson PR, Andresen A, Collins AS, Fowler AR, Fritz H, Ghebreab W, Kusky T, Stern RJ (2011) Late Cryogenian–Ediacaran history of the Arabian-Nubian Shield: a review of depositional, plutonic, structural, and tectonic events in the closing stages of the northern East African Orogen. J Afr Earth Sci 61:167–232

Johnson PR, Kattan F (1999) The timing and kinematics of a suturing event in the northeastern part of the Arabian shield, Kingdom of Saudi Arabia: Saudi Arabian Deputy Ministry for Mineral Resources Open File Report USGS-OF-99-3, 29 p

Johnson PR, Woldehaimanot B (2003) Development of the Arabian-Nubian Shield: Perspectives on accretion and deformation in the northern East African Orogen and the assembly of Gondwana. In: Yoshida M, Dasgupta S, Windley B (eds) Protero-zoic East Gondwana: supercontinent assembly and breakup. Geol Soc Lond, Special Publications 206:289–325

Kelemen PB (1995) Genesis of high Mg # andesites and the continental crust. Contrib Miner Petrol 120:1–19

Kemp AIS, Hawkesworth CJ, Paterson BA, Kinny PD (2006) Episodic growth of the Gondwana supercontinent from hafnium and oxygen isotopes in zircon. Nature 439:580–583

Kennedy AK, De Laeter JR (1994) The performance characteristics of the WA SHRIMP II ion microprobe. U.S. Geological Survey Circular 166:1107

King PL, White AJR, Chappell BW, Allen CM (1997) Characterization and origin of aluminous A-type granites from Lachlan Fold Belt, Southeastern Australia. J Petrol 38:371–391

Kusky T, Matsah MI (2003) Neoproterozoic dextral faulting on the Najd Fault System, Saudi Arabia, preceded sinistral tectonics related to the closure of the Mozambique Ocean. J Geol Soc, Lond 206:327–361 (Special Publications)

Lehmann B, Mahawat C (1989) Metallogeny of tin in central Thailand: a genetic concept. Geology 17:426–429

Liégeois JP, Black R (1987) Alkaline magmatism subsequent to collision in the Pan-African belt of the Adrar des Iforas (Mali). In: Fitton JG, Upton BJG (eds) Alkaline igneous rocks. Geol Soc Lond, Spec Publ 30:381–401

Liégeois JP, Stern RJ (2010) Sr-Nd isotopes and the geochemistry of granite-gneiss complexes from the Meatiq and Hafafit domes, Eastern, Desert, Egypt: No evidence for pre-Neoproterozoic crust. J Afr Earth Sci 57:31–40

Ludwig KR (2001a) SQUID 1.02: a user's manual. Berkeley Geochronology Center, Special Publication No 2, Berkeley, CA, p 19

Ludwig KR (2001b) Users manual for Isoplot/Ex version 2.05. Berkeley Geochronology Center, Special Publication No 1a, Berkeley, CA, p 48

Maniar PD, Piccoli PM (1989) Tectonic discrimination of granitoids. Geol Soc Am Bull 101:636–643

McDonough WF, Sun SS (1995) The composition of the Earth. Chem Geol 120:223–253

Miller CF (1985) Are strongly peraluminous magmas derived from politic sedimentary sources? J Geol 93:673–689

Miller CF, Mittlefehlt DW (1984) Extreme fractionation in felsic magma chambers: a product of liquid-state diffusion or fractional crystallization? Earth Planet Sci Lett 68:151–158

Miller DM, Goldstein SL, Langmuir CH (1994) Cerium/lead and lead isotope ratios in arc magmas and the enrichment of lead in the continents. Nature 368:514–520

Moghazi A-KM, Ali KA, Wilde SA, Zhou Q, Andersen T, Andresen A, Abu El-Enen MM, Stern RJ (2012) Geochemistry, geochronology, and Sr–Nd isotopes of the Late Neoproterozoic Wadi Kid volcano-sedimentary rocks, Southern Sinai, Egypt. Lithos 154:147–165

Moghazi AM, Harbi HM, Ali KA (2011) Geochemistry of the Late Neoproterozoic Hadb adh Dayaheen ring complex, Central Arabian Shield: implications for the origin of rare-metal-bearing post-orogenic A-type granites. J Asian Earth Sci 42:1324–1340

Montero P, Bea F, Corretge LG, Floor P, Whitehouse MJ (2009) U–Pb ion microprobe dating and Sr–Nd isotope geology of the Galiñeiro Igneous Complex. A model for the peraluminous/peralkaline duality of the Cambro-Ordovician magmatism of Iberia. Lithos 107:227–238

Moreno JA, Molina JF, Montero P, Abu Anbar M, Scarrow JH, Cambeses A, Bea F (2014) Unraveling sources of A-type magmas in juvenile continental crust: constraints from compositionally diverse Ediacaran post-collisional granitoids in the Katerina Ring Complex, southern Sinai, Egypt. Lithos 192–195:56–85

Moussa EMM, Stern RJ, Manton WI, Ali KA (2008) SHRIMP zircon dating and Sm/Nd isotopic investigations of Neoproterozoic granitoids, Eastern Desert, Egypt. Precamb Res 160:341–356

Mushkin A, Navon O, Halicz L, Hartmann G, Stein M (2003) The petrogenesis of A-type magmas from the Amram Massif, Southern Israel. J Petrol 44:815–832

Nehlig P, Genna A, Asirfane F (2002) A review of the Pan-African evolution of the Arabian Shield. GeoArabia 7:103–124

Pallister JS, Stacey JS, Fischer LB, Premo WR (1988) Precambrian ophiolites of Arabia; geologic setting, U–Pb geochronology, Pb-isotope characteristics, and implications for continental accretion. Precambr Res 38:1–54

Patiño Douce AE (1997) Generation of metaluminous A-type granitoids by low-pressure melting of calc-alkaline granitoids. Geology 25:743–746

Pearce J (1982) Trace element characteristics of lavas from destructive plate boundaries. In: Thorpe RS (ed) Andesites: orogenic andesites and related rocks. Wiley, pp 525–548

Pearce J, Harris NB, Tindle AG (1984) Trace element discrimination diagrams for the tectonic interpretation of granitic rocks. J Petrol 25:956–983

Roberts MP, Clemens JD (1993) Origin of high potassium, calc-alkaline, I-type granitoids. Geology 21:825–828

Robinson FA, Foden JD, Collins AS, Payne JL (2014) Arabian Shield magmatic cycles and their relationship with Gondwana assembly: Insights from zircon U–Pb and Hf isotopes. Earth Planet Sci Lett 408:207–225

Robinson FA, Foden JD, Collins AS (2015) Geochemical and isotopic constraints on island arc, synorogenic, post-orogenic and anoro-genic granitoids in the Arabian Shield, Saudi Arabia. Lithos 220–223:97–115

Roobol MJ, Ramsay CR, Jackson NJ, Darbyshire DPF (1983) Late Proterozoic lavas of the Central Arabian Shield—evolution of an ancient volcanic arc system. J Geol Soc London 140:185–202

Rosa DRN, Finch AA, Andersen T, Inverno CMC (2009) U–Pb geochronology and Hf isotope ratios of magmatic zircons from the Iberian Pyrite Belt. Mineral Petrol 95:47–69

Rudnick R, Gao S (2003) Composition of the continental crust. Treatise Geochem 3:1–64

Rudnick RL, Gao S, Ling W-L, Liu Y-S, McDonough WF (2004) Petrology and geochemistry of spinel peridotite xenoliths from Hannuoba and Qixia, North China craton. Lithos 77:609–637

Secchi FA, Brotzu P, Callegari E (1991) The Arburese igneous complex (SW Sardinia, Italy)—an example of dominant igneous fractionation leading to peraluminous cordierite-bearing leucogranites as residual melts. Chem Geol 92:213–249

Shervais JW (1982) Ti-V plots and the petrogenesis of modern and ophiolitic lavas. Earth Planet Sci Lett 59:101–118

Sisson TW (1994) Gornblende-melt trace-element partitioning measured by ion microprobe. Chem Geol 117:331–344

Skjerlie KP, Johnston AD (1992) Vapor-absent melting at 10 kbar of a biotite- and amphibole-bearing tonalitic gneiss: implication for the generation of A-type granites. Geology 20:263–266

Stacey JS, Agar RA (1985) U–Pb isotopic direct evidence for the accretion of a continental microplate in the Zalm region of the Saudi Arabian shield. J Geol Soc London 142:1189–1203

Stacey JS, Hedge CE (1984) Geochronologic and isotopic evidence for early Proterozoic crust in the eastern Arabian shield. Geology 12:310–313

Stern RJ (1994) Arc assembly and continental collision in the Neoproterozoic East African Orogen: implications for the consolidation of Gondwanaland. Ann Rev Earth Planet Sci 22:319–351

Stern RJ, Johnson PR (2010) Continental lithosphere pf the Arabian Plate: a geologic, petrologic, and geophysical synthesis. Earth-Sci Rev 101:29–67

Stoeser DB (1986) Distribution and tectonic setting of plutonic rocks of the Arabian Shield. J Afr Earth Sc 4:21–46

Stoeser D, Camp E (1985) Pan-African microplate accretion of the Arabian Shield. Geol Soc Am Bull 96:817–826

Stoeser D, Frost C (2006) Nd, Pb, Sr, and O isotopic characterization of Saudi Arabian Shield terranes. Chem Geol 226:163–188

Streckeisen A, Le Maitre RW (1979) A chemical approximation to the modal QAPF classification of the igneous rocks. N Jb Miner Abh 136:169–206

Sun SS, McDonough WF (1989) Chemical and isotopic systematics of oceanic basalts: implications for mantle composition and processes. In: Saunders AD, Norry MJ (eds) Magmatism in Ocean Basins. Geological Society of London, Special Publications 42:313–345

Sylvester PJ (1998) Post-collisional strongly peraluminous granites. Lithos 45:29–44

Taylor SR, McLennan SM (1985) The continental crust: its composition and evolution. Blackwell Scientific Publishers, Oxford, p 312

Teixeira RJS, Neiva AMR, Gomes MEP, Corfu F, Cuesta A, Croudace IW (2012) The role of fractional crystallization in the genesis of early syn-D3, tin mineralized Variscan two-mica granites from the Carrazeda de Ansiães area, Northern Portugal. Lithos 153:177–191

Tiepolo M, Bottazzi P, Foley SF, Oberti R, Vannucci R, Zanetti A (2001) Fractionation of Nb and Ta from Zr and Hf at mantle depths: the role of titanian pargasite and kaersutite. J Petrol 42:221–232

Turner SP, Foden JD, Morrison RS (1992) Derivation of some Atype magmas by fractionation of basaltic magma: an example from the listvenites Ridge, South Australia. Lithos 28:151–179

Turpin L, Cuney M, Friedrich M, Bouchez JL, Aubertin M (1990) Metaigneous origin of Hercynian peraluminous granites in N.W. French Massif Central: implications for crustal history reconstructions. Contrib Miner Petrol 104:163–172

Wang L-X, Ma C-Q, Zhang C, Zhang J-Y, Marks MAW (2014) Genesis of leucogranite by prolonged fractional crystallization: a case study of the Mufushan complex, South China. Lithos 206–207:147–163

Wetherill GW (1956) Discordant uranium–lead ages I. Trans Am Geophys Union 37:320–326

Whalen JB, Currie KL, Chappell BW (1987) A-type granites: geochemical characteristics, discrimination and petrogenesis. Contrib Miner Petrol 95:407–419

Wiedenbeck M, Allé P, Corfu F, Griffin WL, Meier M, Oberli F, Von Quadt A, Roddick JC, Spiegel W (1995) Three natural zircon standards for U–Th–Pb, Lu–Hf, trace element and REE analyses. Geostand Newsl 19:1–23

Wilde SA, Youssef K (2000) Significance of SHRIMP U–Pb dating of the Imperial Porphyry and associated Dokhan Volcanics, Gebel Dokhan, North Eastern Desert, Egypt. J Afr Earth Sci 31:403–410

Wolf MB, Wyllie PJ (1994) Dehydration-melting of amphibolite at 10 kbar: the effects of temperature and time. Contrib Mineral Petrol 115:369–383

Wormald RJ, Price RC (1988) Peralkaline granites near Temora, Southern New South Wales: tectonic and petrological implications. Aust J Earth Sci 35:209–221

Wu FY, Sun DY, Li H, Jahn BM, Wilde S (2002) A-type granites in northern China: age and geochemical constraints on their petrogenesis. Chem Geol 187:143–173

Xiong XL, Adam J, Green TH (2005) Rutile stability and rutile/melt HFSE partitioning during partial melting of hydrous basalt: implications for TTG genesis. Chem Geol 234:105–126

Zhang Y, Yang J-H, Sun J-F, Zhang J-H, Chen J-Y, Li X-H (2015) Pterogenesis of Jurassic fractionated I-type granites in Southeast China: constraints from whole-rock geochemical and zircon U–Pb and Hf-O isotopes. J Asian Earth Sci 111:268–283

Zhang XH, Yuan LL, Xue FH, Zhang Y (2012) Contrasting Triassic ferron granitoids from northwestern Liaoning, North China: magmatic monitor of Mesozoic decratonization and craton-orogen. Lithos 144–145:12–23